Predicting Regenerative Chatter in Turning Using Operational Modal Analysis

by

Sooyong Kim
B.Sc., Pusan National University, 2012

A Thesis Submitted in Partial Fulfillment of the
Requirements for the Degree of

Master of Applied Science

in the Department of Mechanical Engineering

University of Victoria

Predicting Regenerative Chatter in Turning Using Operational Modal Analysis

by

Sooyong Kim
B.Sc., Pusan National University, 2012

Supervisory Committee

Dr. Keivan Ahmadi, Co-Supervisor
(Department of Mechanical Engineering)

Dr. Martin Byung-Guk Jun, Co-Supervisor
(Department of Mechanical Engineering)

ABSTRACT

Chatter, unstable vibration during machining, damages the tool and workpiece. A proper selection of spindle speed and depth of cut are required to prevent chatter during machining. Such proper cutting conditions are usually determined using vibration models of the machining process.

Nonetheless, uncertainties in modeling or changes in dynamics during the machining operations can lead to unstable machining vibrations, and chatter may arise even when stable cutting conditions are used in the process planning stage. As a result, online chatter monitoring systems are key to ensuring chatter-free machining operations. Although various chatter monitoring systems are described in the literature, most of the existing methods are suitable for detecting chatter after vibrations become unstable. In order to prevent poor surface finish resulting from chatter marks during the finishing stages of machining, a new monitoring system that is capable of predicting the occurrence of chatter while vibrations are still stable is required.

In this thesis, a new approach for predicting the loss of stability during stable turning operations is developed. The new method is based on the identification of the dynamics of self-excited vibrations during turning operations using Operational Modal Analysis (OMA). The numerical simulations and experimental results presented in this thesis confirm the possibility of using Operational Modal Analysis as an online chatter prediction method during stable machining operations.

Contents

List of Tables

List of Figures

ACKNOWLEDGEMENTS

I would like to thank:

My supervisor, Dr. Keivan Ahmadi for his invaluable inspiration and motivation throughout my entire work during my M.ASc. I sincerely appreciate his willingness to help my research and to give advice whenever I have asked . Without his advice, encouragement and support, this work could not have been a reality.

Dr. Martin Byung-guk Jun for giving me a great opportunity that I have successfully studied and completed my M.ASc course in UVIC.

Dynamics and Digital Manufacturing Lab , Mehran Farhadmanesh, Yaser Mohammad, Hamed Assadi, Manish Joddar, Vahid Ostad Ali Akbari and Anahita Habibian for all the encouragements and the helps.

Dr. Jooeun Ahn for providing answers and inspirations with me who finds the right direction in life. His advice enables to achieve my goal and inspires my motivation throughout my life.

I appreciate all the helps from Dr. Jung-hyuk Ko, Yonghyun Cho, Jooyoung Eddie Lee and Seungwon Tim Jun. I would also thank to my beloved father, mother, father in law and mother in law who supported and provided me throughout my whole life. It is my honor to have family members like them. In particular, I would like to thank my wife for her sincere love and supports. I cannot forget to best friends, Taehun Kim, Minwoo Jung, Yongjin Kwon and Bumjo Kim for their supports and encouragements from Korea. Moreover, I thank to Scott Park and Katerine Kang for taking care of our couple like a son and daughter in Victoria. Lastly, I would like to thank God for everything.

DEDICATION

I am dedicating this thesis to my lovely family. I love you.

Chapter 1

Introduction

Various forms of machining such as milling, drilling, and turning constitute a major portion of manufacturing processes in a broad range of applications. Increasing the Material Removal Rate of machining processes is a key objective in optimization of manufacturing processes, which can lead to increased productivity and reduce production cost. Vibrations induced by the machining forces is a main obstacle limiting the increasing of the material removal rate.

1.1 Problem Statement

Regenerative chatter is the unstable vibrations that arise during machining processes if an improper combination of depth of cut and spindle speed is selected. If not prevented, chatter may cause severe damages to the tool, spindle, and the workpiece. Self-excited vibrations due to the feedback between vibrations generated in subsequent cuts is known to be the source of regenerative chatter. To prevent chatter, generally, stable spindle speeds and depth of cuts are usually selected according to the vibration models of the machining process from Stability Lobe Diagrams (SLD). SLD is capable of showing the border between the stable and unstable depth of cuts at each spindle speed. Although selecting stable spindle speed and depth of cut according to SLD has proved to be an effective method to avoid chatter without sacrificing productivity, SLD can be imprecise for various reasons such as un-modeled phenomena or the variation of the system parameters during the process (e.g. increased tool wear). Therefore, even when the spindle speed and depth of cut are selected according to SLD, it is critical to monitor the stability of the system during the process to avoid the damages that may occur because of chatter.

Chatter monitoring systems are commonly used during machining processes to detect the occurrence of chatter and take preventive or corrective actions. Vast majority of the existing chatter detection systems employ a form of signal processing to extract chatter indicators from various sensory data such as vibration, sound, and force. Although the existing methods efficiently detect chatter after it occurs, they are not able to predict its occurrence before vibrations become unstable. Chatter prediction methods are critical for preventing the occurrence of chatter, rather than detecting them, in order to avoid poor surface finish due to chatter marks, particularly in finishing stages of machining.

1.2 Objectives

The objective in this work is to develop a new method to predict the loss of stability of vibrations during machining processes while the process is still stable. In order to achieve this objective, the effectiveness of Operational Modal Analysis methods in the identification of machining dynamics in stable conditions will be studied. The focus of this work will be on turning dynamics, although the developed methods will be extendable to other machining processes as well.

1.3 Thesis Organization

The thesis is structured as follows: In Chapter 2, the main literature and background associated with turning dynamics, modeling regenerative chatter and its stability, and OMA in the presence of harmonics are discussed briefly. In Chapter 3, Multi Degree of Freedom (MDOF) turning model is explained. In addition, Time Domain Poly Reference (TDPR) and modified Least Squares Complex Exponential (LSCE) method used to predict chatter are discussed in Chapter 3. In Chapter 4, numerical Simulation and experimental study is presented to investigate the effectiveness of chatter prediction using OMA methods. In the final chapter, Chapter 5, a summary of the thesis as well as the conclusions are presented.

This thesis is written based on the paper *"Predicting Regenerative Chatter in Turning Using Operational Modal Analysis"* submitted to the journal, *Mechanical Systems and Signal Processing* in 2019.

Chapter 2

Theoretical Background and Literature Review

2.1 Chatter in Turning

In this section, a Single Degree Of Freedom (SDOF) model of turning dynamics and its stability is discussed.

2.1.1 Dynamics of SDOF in turning operation

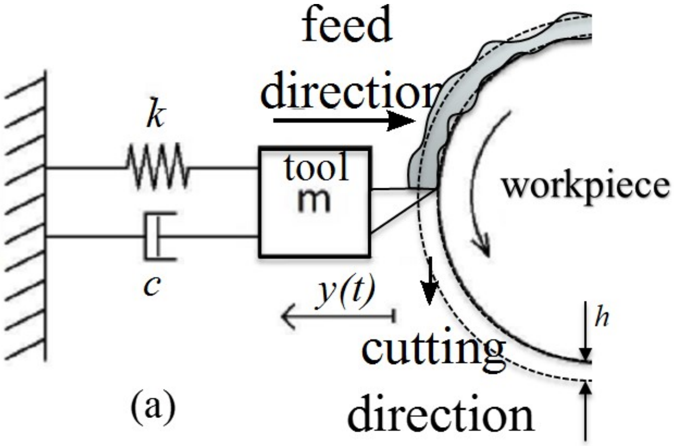

Figure 2.1: SDOF model for the turning operation.

A schematic description of turning operation with a flexible tool is shown in Fig. 2.1. The tool flexibility is represented by an SDOF system in the feed (y) direction. The equation of motion of the SDOF system is described as follows[4]:

$$\begin{aligned} m\ddot{y}(t) + c\dot{y}(t) + ky(t) &= F_y(t) \\ F_y(t) &= K_f a[h - y(t) + y(t-T)] \end{aligned} \tag{2.1}$$

where $y(t)$ is the vibrations of the tool in feed direction and $y(t-T)$ is the waviness left on the machined surface by the vibrations in the previous pass; they are also referred to as the inner and outer vibrations. K_f is the constant cutting force coefficient in feed direction, a is the width of cut, and h is the feed per spindle revolution. The constant T is the spindle revolution period. As shown in Eq. 2.1, the cutting force (F_y) is proportional to the overall chip thickness, which is generated by the feed motion of the tool (h) and modulated by the phase difference between inner and outer vibrations $(y(t-T) - y(t))$. The feed-generated part of the force $(K_f ah)$ does not affect the stability of the system and therefore is eliminated from the equation of motion:

$$m\ddot{y}(t) + c\dot{y}(t) + ky(t) = K_f a[y(t-T) - y(t)] \tag{2.2}$$

Moving the term of the inner vibrations to the left hand side and keeping the outer vibrations at the right hand side leads to the following Delay Differential Equation describing the self-excited vibrations of the tool during machining:

$$m\ddot{y}(t) + c\dot{y}(t) + k_1 y(t) = K_f a y(t-T) \tag{2.3}$$

where, K_1= k + $K_f a$ is the modified stiffness.

2.1.2 Stability Lobes

The self-excited vibrations described by Eq. 2.3 may become unstable if the width of cut (a) and spindle speed $(\frac{60}{T})$ is selected inappropriately [3]. Tobias and Fishwick[47] and Tlusty and Polacek[44] were, concurrently but separately, the first to formulate regenerative chatter and determine the stability of vibrations in cutting processes. As can be seen a regeneration of waviness on the machined surface on the workpiece in Fig. 2.1, the mechanism of regeneration is modified with tool dynamic deflection in the feed rate, $y(t)$. The stability of the self excited vibrations in the turning process is usually presented using

Stability Lobe Diagrams (SLD), which are shown in Fig. 2.2. As shown in this figure, the SLD show the border between stable and unstable width of cut at each spindle speed. In Fig. 2.2, the white area below the border of the lobes shows the stable area but the gray area above the lobes shows the unstable region. Also, the dashed line shows the critical width of cut below which vibrations are stable regardless of the spindle speed.

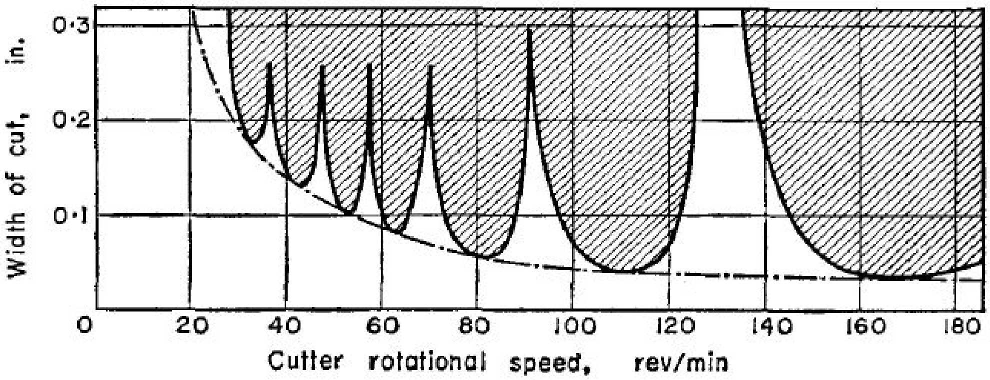

Figure 2.2: Stability chart of machining process carried out on a horizontal milling machine. Chatter arose for only those values of the rotational speed and the depth of cut which correspond to the shaded regions.[46]

In milling operations, self-excited chatter is described using DDE with time periodic coefficients. Tlusty[45] presented a numerical simulation method to analyze chatter in milling. Also, DeVor et al. (1980), Altintas and Spence (1991), and Shin and Water (1994) present numerical simulations including more complex features such as exact chip thickness, cutting force, process damping and tool wear[24]. Altintas et al. developed a frequency domain semi-analytical solution for chatter in milling by assuming that the time-periodic coefficients can be approximated by a finite number of Fourier expansion coefficients[5, 34]. Tang and Liu studied chatter in milling of thin-walled plates and developed a three-dimensional SLD in terms of the spindle speed, axial depth of cut and, the ratio between radial depth and Tool radius[43]. Recently, various numerical methods have been presented to achieve better accuracy and shorter computation time of stability lobes in milling operations[39]. Niu proposed the fourth order Runge-Kutta method (CRKM) and the generalized Runge-Kutta method (GRKM), and Li presented a complete discretization method but both based on classic Runge-Kutta method to predict stability[37, 30]. Also, for high computational efficiency and accuracy, the Simpson method[55], Orthogonal polynomial approximation[53], and Least square approximation[38] have been studied. Most recently, Deng[16] presented stability analysis using robustness evaluation by using the Edge theorem and Zero Exclusion condition based on conventional milling stability models with designing algorithm optimization.

2.1.3 Chatter Stability limits

The closed-loop diagram shown in Fig. 2.3 represents the delayed dynamics of the turning system. The delay term in the feedback loop converts the lumped SDOF system into a distributed parameter system with infinite dimensions. At the certain values of the width of cut, a, and spindle revolution period, T, the closed-loop system in Fig. 2.3 may become unstable and lead to regenerative chatter. The stability of the closed-loop system is determined with respect to to the roots of its characteristic equation (i.e. system poles) shown in Eq. 2.4.

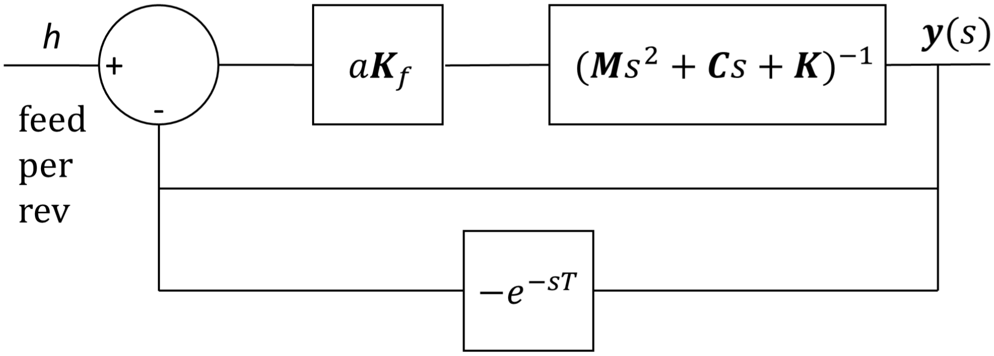

Figure 2.3: Closed loop diagram describing SDOF model of a simple orthogonal machining dynamics

$$1 + (1 - e^{-sT})K_f a\Phi(s) = 0 \tag{2.4}$$

where $\Phi(s) = (ms^2 + cs + k)^{-1}$ is the transfer function of the SDOF system:

$$\Phi(s) = G(s) + jH(s) \tag{2.5}$$

where, G and H are real and imaginary part of Φ respectively. When the roots of the characteristic equation cross the imaginary axis from left side of the complex to the right side, i.e. $s = j\omega_c$, the system become unstable:

$$\begin{aligned} &1 + K_f a\Big\{(1 - cos(\omega_c T))G - sin(\omega_c T)H\Big\} \\ &\quad + jK_f a\Big\{(1 - cos(\omega_c T))H + sin(\omega_c T)G\Big\} = 0 \end{aligned} \tag{2.6}$$

where ω_c is the chatter frequency. Since both the imaginary part and the real part of Eq. 2.6 has to be zero we have two equations. Solving the resulting two equations, after some trigonometric manipulations, yield the following parametric equations of the width of cut and spindle revolution period at the border of stability:

$$a_{lim} = \frac{-1}{2K_f G} \tag{2.7}$$

and

$$T = \frac{2\psi + 3\pi + 2n\pi}{\omega_c} \tag{2.8}$$

where $\psi = \arctan\frac{H}{G}$ and n is an integer number. Stability lobe diagram is obtained by sweeping ω_c in Eqs.2.7 and 2.8 in a wide frequency range and plotting the resulting width of cut and spindle speed, $60/T$ [rev/min].

2.1.4 Impulse Response Function

The response of Linear Time Invariant (LTI) SDOF system in Eq. 2.1 to arbitrary input force is determined as the convolution between the input force, $f(t)$, and the Impulse Response (IR) in Y-direction, $h(t)$:

$$\mathbf{y}(t) = \int_{-\infty}^{t} \mathbf{h}\,(t - \alpha)\mathbf{f}\,(\alpha)\,d\alpha \tag{2.9}$$

The IR can be decomposed into the modal parameters of the system as follows:

$$\mathbf{h}(t) = \sum_{n=1}^{N} \mathbf{A_n} e^{\lambda_n t} + \mathbf{A_n^*} \mathbf{e^{\lambda_n^* t}} \tag{2.10}$$

where, λ_n are the dominant poles of the system that appear in complex conjugate pairs; the $*$ sign stands for complex conjugate. Although the delayed system is infinite dimensional, N dominant poles are considered in Eq. 2.10. Substituting the IR function from Eq. 2.10 into the convolution equation, Eq. 2.9 , the following equation is obtained:

$$\mathbf{y}(t) = \sum_{n=1}^{N} \left(\mathbf{A}_n \int_{-\infty}^{t} e^{\lambda_n (t-\alpha)} \mathbf{f}\left(\alpha\right) d\alpha + \mathbf{A}_n^* \int_{-\infty}^{t} e^{\lambda_n^* (t-\alpha)} \mathbf{f}\left(\alpha\right) d\alpha \right) \tag{2.11}$$

2.2 Operational Modal Analysis

Conventionally, poles of mechanical systems are identified by conducting Experimental Modal Analysis (EMA) [12, 19, 33] where controlled excitation (e.g.impulse hammer) to the structure and the resulting response (e.g.acceleration) are measured and used in various time [10, 18, 50, 52, 1] and frequency [15, 28, 49, 51, 13] domain methods to identify the poles (or modal parameters) of the system. Alternatively, OMA can be used when the measurement of the excitation force is not possible for practical reasons, and therefore only the response of the system to unmeasured operational loads is used to identify its poles.

2.2.1 OMA methods

Modal analysis of wind turbines is one of the most common field of application of OMA, where the traditional EMA method is impossible[48, 2]. Also in the field of machining, OMA is used for in-process modal analysis of the machine tool [54, 21, 29]. The Frequency Domain Decomposition (FDD) also known as Peak Picking is a non-parametric technique. The FDD does not rely on any type of curve fitting based on parametric modeling and it is easy and fast to use. However, a disadvantage of FDD is that the damping at each mode is not estimated. Moreover, the frequency resolution is not better than using the FFT line spacing[20]. The Enhanced Frequency Domain Decomposition (EFDD) technique is an extension of FDD. EFDD provides an improved estimation of not only the natural frequencies but also its mode shapes and damping ratios. The key step in the Stochastic Subspace Identification (SSI) technique is the projection of the row space of the future outputs into the

Table 2.1: Consequences of harmonic components for various identification techniques[23]

Technique	**Consequences**
All technique	• Harmonic components are potentially mistaken for being structural modes • Harmonic components might potentially bias the estimation of the structural modes (natural frequency, modal damping, mode shape) • A high dynamic range might be required to extract "weak" modes
FDD	• The picked FFT line might be biased by the harmonic component(s) • Harmonics must be away from the structural modes (only the picked FFT line is used in the FDD technique)
EFDD	• The identified SDOF function used for modal parameter estimation may be biased by the harmonic component(s) • Harmonic components must be outside the SDOF function thereby potentially narrowing the SDOF function and resulting in poorer identification
SSI	• The SSI methods estimate both harmonic components and structural modes.The modes are estimated correctly even for harmonic components close to or with the equal frequency as the modes • Information in the time signal is used both to extract the harmonic components and the modes, therefore, the recording time should generally be longer

row space of the past outputs. Juang and Pappa [25] suggested modal identification using Singular Value Decomposition (SVD) with the Eigensystem Realization Algorithm (ERA) in 1985. A parametric model is a mathematical model which has several parameters that can be adjusted to change how the model fits into the data. Typically, a set of parameters is decided by minimizing the variance between the expected system response and the measured system response which is often referred to as model calibration[40].

In many applications, in addition to random ambient noise, harmonic excitation is also present in the measured system response. Table 2.1 summarizes the consequence of having harmonic excitation on the results of OMA when various identification methods are used. In general, harmonic components cannot be removed by simple filtering. In most cases, filtering significantly changes the pole of the actual structural mode, which causes the mathematical results of natural frequency and modal damping to vary widely.

Mohanty identified modal parameters in the presence of harmonic excitation using the poly reference least-square complex exponential (LSCE) method in the time-domain[35]. Recently, Brandt also applied the developed LSCE method to analyze the 3DOF system in the harmonic presence and remove harmonic components using order domain deletion technique[7]. Transmissibility Function-Based method (TFB) is developed using the white noise excitation assumption from SSI technique[32]. Also, Operational Modal Analysis based on harmonic excitation (OMAH) is developed and verified using the frequency response thus obtained between harmonic force and response to scale the modal model[9, 8].

2.2.2 Correlation Function

The correlation function (CF) represents a statistical correlation between arbitrary variables. The CF of a signal with itself is referred to as auto CF and is defined as follows:

$$\mathbf{R}_y(T) = \mathrm{E}\left[\mathbf{y}\left(t\right)\mathbf{y}^T\left(t+T\right)\right] \tag{2.12}$$

where E[.] denotes the expected value. Power Spectral Density function (PSD), $G_y(\omega)$, is defined as the Fourier transformation of the correlation function:

$$\mathbf{G}_y\left(\omega\right) = \frac{1}{2\pi}\int\limits_{-\infty}^{+\infty}\mathbf{R}_y\left(T\right)e^{-i\omega T}dT \tag{2.13}$$

When the response expressed by Eq. 2.11 is substituted into the definition of CF in Eq. 2.12, the decomposed expression of the CF is obtained as follows:

$$\mathbf{R}_y\left(T\right)=\sum_{n=1}^{N}\sum_{s=1}^{N}\left(\begin{array}{l}\mathbf{A}_n\int\limits_{-\infty}^{t}\int\limits_{-\infty}^{t}e^{\lambda_n(t-\alpha)}e^{\lambda_s(t+T-\beta)}\mathrm{E}[\mathbf{f}(\alpha)\mathbf{f}^T(\beta)]d\beta d\alpha\mathbf{A}_s+\\ \mathbf{A}_n\int\limits_{-\infty}^{t}\int\limits_{-\infty}^{t}e^{\lambda_n(t-\alpha)}e^{\lambda_s^*(t+T-\beta)}\mathrm{E}[\mathbf{f}(\alpha)\mathbf{f}^T(\beta)]d\beta d\alpha\mathbf{A}_s^*+\\ \mathbf{A}_n^*\int\limits_{-\infty}^{t}\int\limits_{-\infty}^{t}e^{\lambda_n^*(t-\alpha)}e^{\lambda_s(t+T-\beta)}\mathrm{E}[\mathbf{f}(\alpha)\mathbf{f}^T(\beta)]d\beta d\alpha\mathbf{A}_s+\\ \mathbf{A}_n^*\int\limits_{-\infty}^{t}\int\limits_{-\infty}^{t}e^{\lambda_n^*(t-\alpha)}e^{\lambda_s^*(t+T-\beta)}\mathrm{E}[\mathbf{f}(\alpha)\mathbf{f}^T(\beta)]d\beta d\alpha\mathbf{A}_s^*\end{array}\right) \tag{2.14}$$

When the force that is applied in Y-direction (cutting force) is white noise, its CF can be a scaled delta function in $M \times M$ dimension:

$$\mathrm{E}\left[\mathbf{f}\left(\alpha\right)\mathbf{f}^T\left(\beta\right)\right]=F_0\delta\left(\beta-\alpha\right)\mathbf{I}_{M\times M} \tag{2.15}$$

where F_0, a constant, is proportional to the variance of the input force and its frequency bandwidth and I is an identity matrix of M dimensions. Therefore, the CF of the response when the system is subjected to white noise excitation can be decomposed into the modal form similar to IR function in Eq. 2.14:

$$\mathbf{R}_y\left(T\right)=\sum_{n=1}^{N}\left(\mathbf{P}_n e^{\lambda_n T}+\mathbf{P}_n^* e^{\lambda_n^* T}\right) \tag{2.16}$$

where P_n and $P^*{}_n$ are constant complex conjugate pairs and depend on the variance and the bandwidth of the cutting force.

2.3 Chatter Monitoring

Timely detection of chatter is essential in machining processes, particularly in the finishing stages. Cao et al.[14] proposed a new chatter detection method for milling in finishing stage. In their method, the vibration signal was analyzed using Ensemble Empirical Mode Decomposition (EEMD) considering the nonlinear and unstable characteristics of the chatter vibration in the milling process, and the two nonlinear indicators were used for chatter detection. As the severity of the chatter increase, the periodic chatter component gradually dominates, and the ratio of the stochastic noise decreases. In high-speed machining, the chatter monitoring system was developed based on the analysis of cutting forces and Instantaneous Angular Speeds (IAS). By using instantaneous angular velocity-based indicators additional sensors are not required, making it suitable for developing a low-cost monitoring system for chatter detection[27]. Chatter is also detected by monitoring cutting force [36]. Furthermore, Time Domain (TD) algorithm was proposed to facilitate chatter suppression. Time Domain methods are advantageous because they can accurately determine the dominant chatter frequency without using frequency domain, which requires a more transformation such as Fourier transforms[31]. Nonetheless, the vast majority of the existing methods detect chatter only after vibrations become unstable. Although the timely detection of chatter after its occurrence is important for preventing severe damages to the tool or the machine, damages to the workpiece will not be prevented by the existing methods, because chatter marks will leave an imprint on the finished surface. In this thesis, a new approach to monitoring chatter is presented. In the presented approach, the stability margin of the system when it is still stable is determined from the vibrations measured during the process. A similar approach has recently been presented by Kiss et al.[26], where milling dynamics has been approximated by a lumped system, and then an experimental method is used to identify the dominant characteristic multiplier of the system from its response to an impulse applied during the milling process. Monitoring the modulus of the dominant characteristic multiplier of the stable system can be used to forecast the loss of stability of the system before it becomes unstable. In the case study presented in [26], the workpiece is the flexible component and the tool is assumed to be rigid. Therefore, the impulse is applied to the stationary workpiece and the response is also measured using accelerometers installed on the workpiece. Although the method in [26] can effectively determine the stability margin of the system while it is stable, applying impulse on the tool or the workpiece during the process may introduce technical challenges in practical applications.

Chapter 3

Numerical Simulations[1]

3.1 Turning Dynamics

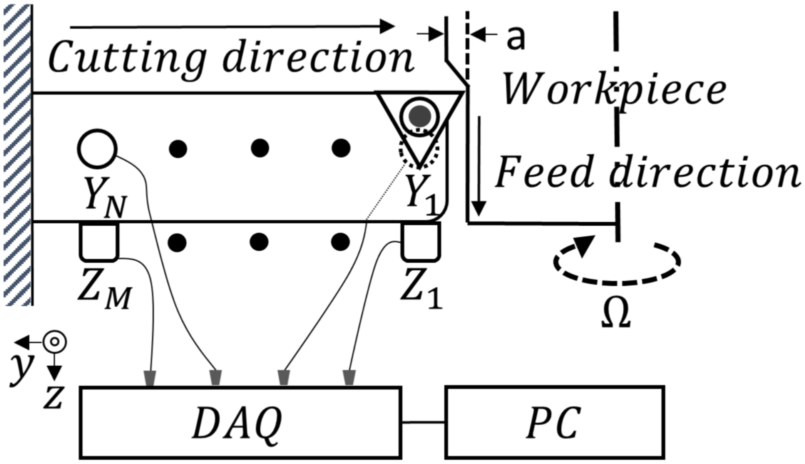

Figure 3.1: MDOF model for the turning process.

Fig. 3.1 shows the Multi Degree Of Freedom (MDOF) system describing the dynamics of the turning tool in the feed (z) and cutting (y) directions. The tool is assumed to be rigid in the axial (x) direction. The tool deflection in the feed direction is represented by the deflections at M discrete points $(z_1, ..., z_M)$ and its deflection in the cutting direction (y) is represented by the deflections of N discrete points $(y_1, ..., y_N)$. In total the model has $D = M + N$ degrees of freedom. The equation governing the motion of the MDOF system is as

---

[1] This chapter is under review for journal publication April 15, 2019

follows:

$$\mathbf{M}\ddot{\mathbf{y}} + \mathbf{C}\dot{\mathbf{y}} + \mathbf{K}\mathbf{y} = \mathbf{F}(t) \tag{3.1}$$

Where $\mathbf{y}$ contains the deflections at the D degrees of freedom

$$\mathbf{y}(t) = \begin{bmatrix} z_1(t) & ... & z_M(t) & y_1(t) & ... & y_N(t) \end{bmatrix}^T \tag{3.2}$$

and $\mathbf{M}$, $\mathbf{K}$, and $\mathbf{C}$ are the corresponding $D \times D$ mass, stiffness, and damping matrices of the MDOF system, respectively. The force vector, $\mathbf{F}(t)$, consists of the cutting forces in feed ($F_z(t)$) and cutting ($F_y(t)$) directions that are applied at y_1 and z_1:

$$\mathbf{F}(t) = \begin{bmatrix} F_z(t) & 0_{1\times(M-1)} & F_y(t) & 0_{1\times(N-1)} \end{bmatrix}^T \tag{3.3}$$

The cutting forces are proportional to the uncut chip thickness generated by the rigid body motion of the tool in feed direction per one revolution of the workpiece (feedrate [mm/rev]) and by the oscillations of the tool around its equilibrium point. The static part of the force generated by the feed motion does not affect its stability and can be easily superimposed to the dynamic solution, therefore it is neglected in what follows. However, due to inherent rotating nature of the process, the static forces will cause strong harmonic excitation in the system that will need to be dealt with in Operational Modal Analysis. The dynamic component of the cutting forces is expressed in terms

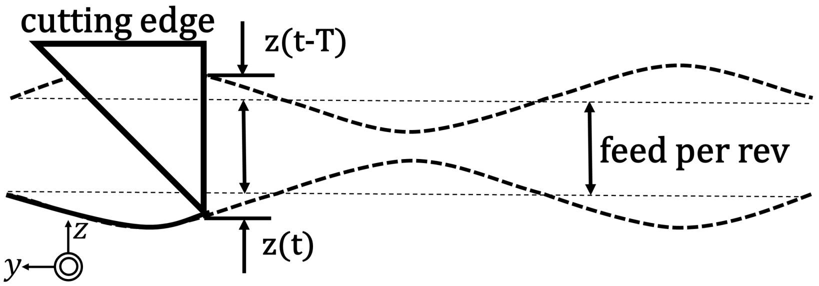

Figure 3.2: Waviness in Turning process according to previous and present cut

of the instantaneous, $\mathbf{y}(t)$, and delayed, $\mathbf{y}(t-T)$, vibrations as follows:

$$\begin{aligned} &\mathbf{F}(t) = \mathbf{K}_c a\{\mathbf{y}(t-T) - \mathbf{y}(t)\} \\ &\mathbf{K}_c = [k_{ij}]\,; \qquad k_{ij} = \begin{cases} K_f & i=1, j=1 \\ K_t & i=M+1, j=1 \\ 0 & \text{otherwise} \end{cases} \end{aligned} \tag{3.4}$$

where $\mathbf{K}_c$ is a square $D \times D$ matrix, and K_f and K_t are the constant cutting force coefficients in feed (z) and cutting (y) directions, respectively. These coefficients are usually determined empirically for each material and cutting tool [3]. The width of cut is denoted a. The delay term ($\mathbf{y}(t-T) - \mathbf{y}(t)$) in Eq. 3.4 represents the modulation of the chip thickness due to the vibrations in the feed direction ($z(t)$) and the waviness left on the surface by of the vibrations at the previous pass ($z(t-T)$), where T is the spindle revolution period. Modulation of the constant chip thickness (feed per revolution) by the oscillation in the feed direction is presented in Fig. 3.2. Substituting the cutting force from Eq. 3.4 in the governing equation of the MDOF system in Eq. 3.1 results in the following Delay Differential Equation describing the dynamics of regenerative vibrations in turning.

$$\mathbf{M}\ddot{\mathbf{y}} + \mathbf{C}\dot{\mathbf{y}} + \bar{\mathbf{K}}\mathbf{y} = \mathbf{K}_c a\mathbf{y}(t-T); \quad \bar{\mathbf{K}} = \mathbf{K} + \mathbf{K}_c a \tag{3.5}$$

Fig. 3.3 shows the closed loop diagram representing the delayed dynamics of the turning system. The presence of the delay term in the feedback loop needs to be converted into the lumped MDOF system from a distributed parameter system. Depending on the values of the width of cut, a, and spindle revolution period, T, the closed loop system in Fig. 3.3 may become unstable and lead to regenerative chatter.

3.2 Discrete Time Domain Model

Various discretization schemes have been used in the literature to approximate the distributed system in Eq. 3.5 by a finite dimensional lumped system [22, 17]. To solve the problem, the Semi-Discretization Method (SDM)[22] is used to convert the DDE in Eq. 3.5 into a system of Ordinary Differential Equations. In this method, the duration of the delay period (T) is discretized

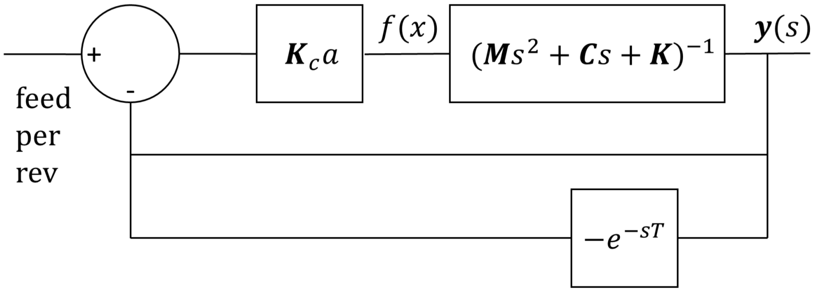

Figure 3.3: Closed loop diagram describing self-excited vibration in turning

into equal time segments of length h such that $T = (r + \frac{1}{2})h$, where r is an integer number. During each time interval $t_i \leq t < t_{i+1}$, the delay term in Eq. 3.5 is assumed to be constant $\mathbf{y}(t_{i-r})$, converting the delay differential equation into a differential equation with step input in each interval:

$$\mathbf{M}\ddot{\mathbf{y}} + \mathbf{C}\dot{\mathbf{y}} + \bar{\mathbf{K}}\mathbf{y} = \mathbf{K}_f a\mathbf{y}(t_{i-r}); \quad t_i \leq t < t_{i+1} \tag{3.6}$$

It was shown in [22] that when r goes to infinity and h goes to zero, Eq. 3.6 converges to the original DDE in Eq. 3.5. The solution of Eq. 3.6 after applying the boundary values of $\mathbf{y}(\mathbf{t})$ at t_i and t_{i+1} results in the following equation that describes the discrete time finite dimensional equivalent of the distributed parameter system shown in Eq. 3.5:

$$\begin{aligned} &\mathbf{u}_{i+1} = \mathbf{G}\mathbf{u}_i \\ &\mathbf{y}_i = \mathbf{P}\mathbf{u}_i; \qquad \mathbf{P} = \left[\begin{array}{cccc} \mathbf{I} & \mathbf{0} & \cdots & \mathbf{0} \end{array}\right]_{D\times(D.(r+2))} \end{aligned} \tag{3.7}$$

where $\mathbf{I}$ and $\mathbf{0}$ are $D \times D$ identity and zero matrices, and $\mathbf{u}_i$ is the discrete time state vector consisting of the displacement and velocities at time steps within one delay period (i.e. spindle revolution period, T):

$$\mathbf{u}_i = \left[\begin{array}{cccccc} \mathbf{y}_{i+1}^T & \dot{\mathbf{y}}_{i+1}^T & \mathbf{y}_i^T & \mathbf{y}_{i-1}^T & \cdots & \mathbf{y}_{i-r+1}^T \end{array}\right]^T \tag{3.8}$$

Here, the superscript T indicates the transpose of a matrix or vector. and $\mathbf{G}$ is the state transition matrix that advances the state vector, $\mathbf{u}_i$, by one time step to, $\mathbf{u}_{i+1}$. The transition matrix depends on the mass, stiffness, and damping matrices of the system, width of cut, cutting force coefficients, and the discretization time interval. To gain the $\mathbf{G}$ matrix, the complete solution

of the ODE in Eq. 3.6 is required.
Rewrite Eq. 3.6 including the homogeneous and particular solutions, is as follows:

$$\begin{aligned}
&\mathbf{y(t)} = \boldsymbol{\Psi\Lambda}\mathbf{c_1} + \boldsymbol{\Psi\Lambda}^*\mathbf{c_2} + \overline{\mathbf{K}}^{\mathbf{-1}}\mathbf{K_c a y_{i-r}};\\
&\boldsymbol{\Lambda} = \mathbf{diag}(\mathbf{e}^{\lambda_\mathbf{1}\mathbf{t}}, ..., \mathbf{e}^{\lambda_\mathbf{N}\mathbf{t}}); \quad \lambda_\mathbf{1} = -\xi_\mathbf{1}\omega_\mathbf{1} + \mathbf{j}\omega_\mathbf{1}\sqrt{\mathbf{1} - \xi_\mathbf{1}^\mathbf{2}};\\
&\boldsymbol{\Psi} = [\boldsymbol{\Psi}_\mathbf{1} \quad \cdots \quad \boldsymbol{\Psi}_\mathbf{N}]
\end{aligned} \tag{3.9}$$

where $\Psi_l, l = 1...N$ are the mass normalized mode shapes of the tool and ω_l and ξ_l are the corresponding modal frequency and damping ratio. The total number of modes considered in the solution are N, and proportional damping is assumed. The constant vectors, c_1 and c_2 are determined by applying the boundary values of $\mathbf{y(t)}$ and its time derivative at $t = ti$:

$$\begin{aligned}
&\mathbf{c_1} = \boldsymbol{\Lambda}_\mathbf{i}^{\mathbf{-1}}\boldsymbol{\Psi}^{\mathbf{-1}}(\mathbf{y_i} - \mathbf{Psi}(\overline{\boldsymbol{\Lambda}}_\mathbf{2} - \overline{\boldsymbol{\Lambda}}_\mathbf{1})^{\mathbf{-1}}\boldsymbol{\Psi}^{\mathbf{-1}}\big(\dot{\mathbf{y}}_\mathbf{i} - \boldsymbol{\Psi}\overline{\boldsymbol{\Lambda}}_\mathbf{1}\boldsymbol{\Psi}^{\mathbf{-1}}(\mathbf{y_i} - \overline{\mathbf{K}}^{\mathbf{-1}}\mathbf{K_c a y_{i-r}})\big)\\
&\qquad -\overline{\mathbf{K}}^{\mathbf{-1}}\mathbf{K_c a y_{i-r}};\\
&\mathbf{c_2} = \boldsymbol{\Lambda}_\mathbf{i}^{*\mathbf{-1}}(\overline{\boldsymbol{\Lambda}}_\mathbf{2} - \overline{\boldsymbol{\Lambda}}_\mathbf{1})^{\mathbf{-1}}\boldsymbol{\Psi}^{\mathbf{-1}}\Big(\dot{\mathbf{y}}_\mathbf{i} - \boldsymbol{\Psi}\overline{\boldsymbol{\Lambda}}_\mathbf{1}\boldsymbol{\Psi}^{\mathbf{-1}}(\mathbf{y_i} - \overline{\mathbf{K}}^{\mathbf{-1}}\mathbf{K_c a y_{i-r}})\Big);\\
&\boldsymbol{\Lambda}_\mathbf{i} = \boldsymbol{\Lambda}(\mathbf{t_i})
\end{aligned} \tag{3.10}$$

where $\overline{\boldsymbol{\Lambda}}_1 = \overline{\boldsymbol{\Lambda}}_1^* = diag(\lambda_1, \cdots, \lambda_N)$. The displacement vector and its derivative at the next time step, t_{i+1}, are obtained by substituting the constants, $\mathbf{c_1}$ and $\mathbf{c_2}$, from Eq. 3.10 in Eq. 3.9:

$$\begin{aligned}
\mathbf{y_{i+1}} &= \mathbf{P_{11}y_i} + \mathbf{P_{12}}\dot{\mathbf{y}}_\mathbf{i} + \mathbf{R_1 y_{i-r}}\\
\dot{\mathbf{y}}_\mathbf{i+1} &= \mathbf{P_{21}y_i} + \mathbf{P_{22}}\dot{\mathbf{y}}_\mathbf{i} + \mathbf{R_2 y_{i-r}}
\end{aligned} \tag{3.11}$$

where

$$\begin{aligned}
\mathbf{P_{11}} &= \boldsymbol{\Psi}(\boldsymbol{\Lambda}_\mathbf{h}\overline{\boldsymbol{\Lambda}}_\mathbf{2} - \boldsymbol{\Lambda}_\mathbf{h}^*\overline{\boldsymbol{\Lambda}}_\mathbf{1})(\overline{\boldsymbol{\Lambda}}_\mathbf{2} - \overline{\boldsymbol{\Lambda}}_\mathbf{1})^{\mathbf{-1}}\boldsymbol{\Psi}^{\mathbf{-1}}\\
\mathbf{P_{12}} &= \boldsymbol{\Psi}(\boldsymbol{\Lambda}_\mathbf{h}^* - \boldsymbol{\Lambda}_\mathbf{h})(\overline{\boldsymbol{\Lambda}}_\mathbf{2} - \overline{\boldsymbol{\Lambda}}_\mathbf{1})^{\mathbf{-1}}\boldsymbol{\Psi}^{\mathbf{-1}}\\
\mathbf{P_{21}} &= \boldsymbol{\Psi}\boldsymbol{\Lambda}_\mathbf{1}\overline{\boldsymbol{\Lambda}}_\mathbf{2}(\boldsymbol{\Lambda}_\mathbf{h} - \boldsymbol{\Lambda}_\mathbf{h}^*)(\overline{\boldsymbol{\Lambda}}_\mathbf{2} - \overline{\boldsymbol{\Lambda}}_\mathbf{1})^{\mathbf{-1}}\boldsymbol{\Psi}^{\mathbf{-1}}\\
\mathbf{P_{22}} &= \boldsymbol{\Psi}(\boldsymbol{\Lambda}_\mathbf{h}^*\overline{\boldsymbol{\Lambda}}_\mathbf{2} - \boldsymbol{\Lambda}_\mathbf{h}\overline{\boldsymbol{\Lambda}}_\mathbf{1})(\overline{\boldsymbol{\Lambda}}_\mathbf{2} - \overline{\boldsymbol{\Lambda}}_\mathbf{1})^{\mathbf{-1}}\boldsymbol{\Psi}^{\mathbf{-1}}\\
\mathbf{R_1} &= \boldsymbol{\Psi}(\mathbf{1} + (\boldsymbol{\Lambda}_\mathbf{h}^*\overline{\boldsymbol{\Lambda}_\mathbf{1}} - \boldsymbol{\Lambda}_\mathbf{h}\overline{\boldsymbol{\Lambda}_\mathbf{2}})(\overline{\boldsymbol{\Lambda}}_\mathbf{2} - \overline{\boldsymbol{\Lambda}}_\mathbf{1})^{\mathbf{-1}})\boldsymbol{\Psi}^{\mathbf{-1}}\overline{\mathbf{K}}^{\mathbf{-1}}\mathbf{K_c a}\\
\mathbf{R_2} &= \boldsymbol{\Psi}(\mathbf{1} + \overline{\boldsymbol{\Lambda}}_\mathbf{1}\overline{\boldsymbol{\Lambda}}_\mathbf{2}(\boldsymbol{\Lambda}_\mathbf{h}^* - \boldsymbol{\Lambda}_\mathbf{h})(\overline{\boldsymbol{\Lambda}}_\mathbf{2} - \overline{\boldsymbol{\Lambda}}_\mathbf{1})^{\mathbf{-1}})\boldsymbol{\Psi}^{\mathbf{-1}}\overline{\mathbf{K}}^{\mathbf{-1}}\mathbf{K_c a}
\end{aligned} \tag{3.12}$$

According to Eq. 3.12, the components of the transition matrix, $\mathbf{G}$, in Eq. 3.7 are obtained as follows:

$$\mathbf{G} = \begin{bmatrix} \mathbf{P}_{11} & \mathbf{P}_{12} & \mathbf{0} & \mathbf{0} & \dots & \mathbf{0} & \mathbf{R}_1 \\ \mathbf{P}_{21} & \mathbf{P}_{22} & \mathbf{0} & \mathbf{0} & \dots & \mathbf{0} & \mathbf{R}_2 \\ \mathbf{I} & \mathbf{0} & \mathbf{0} & \mathbf{0} & \dots & \mathbf{0} & \mathbf{0} \\ \mathbf{0} & \mathbf{0} & \mathbf{I} & \mathbf{0} & \dots & \mathbf{0} & \mathbf{0} \\ \vdots & & & & \ddots & & \vdots \\ \mathbf{0} & \mathbf{0} & \mathbf{0} & \mathbf{0} & \dots & \mathbf{I} & \mathbf{0} \end{bmatrix} \tag{3.13}$$

Equation 3.7 describes the free vibrations (or impulse response) of the regenerative system in discrete time domain. The impulse (or free) response of the finite dimensional system in Eq. 3.7 can also be expressed in modal form in terms of the poles of the discretized system:

$$\mathbf{y}_i = \sum_{p=1}^{2P} c_p \mathbf{a_p} \mu_p^i; \quad \mu_p = e^{\lambda_p h}; \quad \mathbf{a_p} = \mathbf{P}\mathbf{v_p} \tag{3.14}$$

where μ_p are the eigenvalues of the transition matrix and they represent the discrete time poles of the system. The corresponding continues time poles are $\lambda_p = -\xi_p\omega_p + j\omega_p\sqrt{1-\xi_p^2}$, where ω_p and ξ_p are the modal frequency and damping ratio associated with each pole, $\mathbf{a_p}$ are complex mode shapes, and c_p are constants depending on the initial conditions of the free decay. The total number of poles considered in approximating the IR is $2P$, consisting of P pairs of complex conjugate modes. The stability of the discrete time system in Eq. 3.7 is determined with respect to the modulus of the discrete time poles, μ_p. If all of the eigenvalues of the transition matrix (i.e. discrete time poles) are located inside of the unit circle on the complex plane, the system is stable, otherwise, it is unstable. Equivalently, if the damping ratio of any of the corresponding continues time poles, λ_p, are negative, the system is unstable. Therefore, in this work, we consider the smallest modal damping ratio of the system as the measure of its stability. The decline of the smallest modal damping ratio indicates the declining trend of the stability of the machining process.

Chatter prediction methods such as [42] employ the mass, stiffness, and damping matrices of the tool model along with the cutting force coefficients in Eq.

3.7 to determine the stability of vibrations based on the eigenvalues of the resulting transition matrix. In an inverse approach, in this work, we will use System Identification methods to determine the frequency and damping ratio of the modes of the system from vibration signals measured directly during stable turning processes. However, the measurement of the IR of the system ($\mathbf{y_i}$) during machining operations (e.g. using impulse hammer tests) is not practical and thus the IR in Eqs. 3.7 and 3.14 are approximated using the Correlation Function (CF) of the vibration signals measured during the process.

When the lumped system in Eq. 3.7 is subjected to white noise excitation, the Correlation Function (CF) of the response is a scaled equivalent of the system IR (or free decay)[11]. Let us assume that the system in Eq. 3.7 is subjected to normally distributed white noise excitation, and the response of the system, $\bar{\mathbf{y}}_\mathbf{i} = \bar{\mathbf{y}}(\mathbf{t_i})$, is measured at $i = 1...L$ discrete time instants. The CF of the measured response, $\mathbf{R_y}(i)$, in the discrete time domain is defined as follows:

$$\mathbf{R}_y(i) = \frac{1}{(L-i)} \sum_{k=1}^{L-i} \bar{\mathbf{y}}_k \bar{\mathbf{y}}_{k+i}^T; \quad i = 0 \cdots L-1 \tag{3.15}$$

Each column of Ry(i) in Eq. 3.15 is a scaled equivalent of the response, $\mathbf{y_i}$,to an impulse applied at the corresponding DOF[11]. Therefore, similar to the IR in Eq. 3.14, the CF can also be decomposed in terms of the poles of the system in Eq. 3.7:

$$\mathbf{R}_y(i) = \sum_{p=1}^{2P} \mathbf{B}_p \mu_p^i; \quad \mathbf{B_p} = \mathbf{b_p} \mathbf{b_p^T} \tag{3.16}$$

where $\mathbf{b_p}$ is the deflection shape vector corresponding to the mode shapes of the system, $\mathbf{a_p}$.

In the next section, two OMA methods are used to identify the poles (μ_p) of the lumped system in Eq. 3.16 from the CF of the vibration signals measured during the process.

3.3 System Identification

3.3.1 Auto Regressive Model of Correlation Function

The free decay (or IR) of lumped systems such as the system in Eq. 3.7 can be described by Auto Regressive (AR) models in discrete time domain [33]. Since the CF will be used to represent scaled IR in this work, similarly, an AR model is used to describe the CF in discrete time domain:

$$\mathbf{R}_y\left(i\right) = \mathbf{A}_1\mathbf{R}_y\left(i-1\right) + \mathbf{A}_2\mathbf{R}_y\left(i-2\right) + ... + \mathbf{A}_{na}\mathbf{R}_y\left(i-na\right) \tag{3.17}$$

Where $\mathbf{A_1}...\mathbf{A_{na}}$ are the coefficients of the AR model of order na. The AR model can also be expressed in companion form as follows:

$$\mathbf{U}_d\left(i+1\right) = \mathbf{\Phi}\mathbf{U_d}\left(\mathbf{i}\right); \tag{3.18}$$

where $\mathbf{U_d}(\mathbf{i})$ is composed of the CF matrices at na consecutive time steps:

$$\mathbf{u}_d\left(i\right) = \begin{bmatrix} \mathbf{R}_y^T(i-na+1) & \cdots & \mathbf{R}_y^T(i-1) & \mathbf{R}_y^T(i) \end{bmatrix}^T \tag{3.19}$$

and $\mathbf{\Phi}$ is the companion matrix corresponding to the na order AR model in Eq. 3.17:

$$\mathbf{\Phi} = \begin{bmatrix} \mathbf{0} & \mathbf{I} & \mathbf{0} & \mathbf{0} & \mathbf{0} \\ \mathbf{0} & \mathbf{0} & \mathbf{I} & \mathbf{0} & \mathbf{0} \\ \vdots & \vdots & & \ddots & \vdots \\ \mathbf{0} & \mathbf{0} & \mathbf{0} & \mathbf{0} & \mathbf{I} \\ \mathbf{A}_{na} & \mathbf{A}_{na-1} & \cdots & \mathbf{A}_2 & \mathbf{A}_1 \end{bmatrix} \tag{3.20}$$

Substituting one term from the modal expansion of the CF in Eq. 3.16 into Eq. 3.18 leads to the following eigenvalue equation, which shows that the eigenvalues of the companion matrix are also the discrete poles of the system in Eq. 3.7:

$$\mathbf{\Phi}\mathbf{Z_p} = \mu_\mathbf{p}\mathbf{Z_p}; \quad \mathbf{Z_p} = [\ \mathbf{B}_p^T\mu_p^{i-na-1} \ \ \ldots \ \ \mathbf{B}_p^T\mu_p^{i-1} \ \ \mathbf{B}_p^T\mu_p^{i}\ ]^\mathbf{T} \tag{3.21}$$

In the next section, the coefficients of the AR model are determined from the CF of the vibrations measured during turning process, and then the poles of the system are determined as the eigenvalues of the corresponding companion matrix.

3.3.2 Time Domain Poly Reference (TDPR) identification

In this method, also known as Time Domain Poly Reference (TDPR)[11] , the coefficients of the AR model of the CF are determined using the Least Squares approximation of the measured CF. Assuming that the order of the AR model representing the CF is na, the CF in each time step can be expressed as a linear combination of the CF in na preceding time steps as follows: Because the excitation forces are only applied on y_1 and z_1, these DOFs are considered as the references and therefore $\mathbf{R_y(n)}$ in the AR model are $D \times 2$ matrices consisting of the first and $M+1$ column of the full $D \times D$ CF matrix. Consequently, the coefficients in the AR model, $\mathbf{A_j}$, are $D \times D$ matrices. By repeating Eq. 3.17 for np consecutive time steps, the following Hankel form matrix equation is obtained:

$$\mathbf{H}_1^T \mathbf{A}^T = \mathbf{H}_2^T \tag{3.22}$$

where $\mathbf{A}$ contains the coefficients of the AR model, $\mathbf{H_1}$ is the Hankel block matrix consisting of CF at discrete time steps, and $\mathbf{H_2}$ is the row matrix vector of the CF at time step $na+1$ to np:

$$\mathbf{A} = [\ \mathbf{A}_1 \quad \mathbf{A}_2 \quad ... \quad \mathbf{A}_{na}\ ] \tag{3.23}$$

$$\mathbf{H}_1 = \begin{bmatrix} \mathbf{R}_y(1) & \mathbf{R}_y(2) & \dots & \mathbf{R}_y(np-na) \\ \mathbf{R}_y(2) & \mathbf{R}_y(3) & & \mathbf{R}_y(np-(na-1)) \\ \vdots & & \ddots & \vdots \\ \mathbf{R}_y(na) & \mathbf{R}_y(na+1) & & \mathbf{R}_y(np-1) \end{bmatrix} \tag{3.24}$$

$$\mathbf{H}_2 = \begin{bmatrix} \mathbf{R}_y(na+1) & \mathbf{R}_y(na+2) & \cdots & \mathbf{R}_y(np) \end{bmatrix} \tag{3.25}$$

The Least Squares (LS) approximation of $\mathbf{A}$ is obtained using the pseudo-inverse of the Hankel matrix, $\mathbf{H_1}$:

$$\hat{\mathbf{A}} = \mathbf{H}_2 \mathbf{H}_1^+ \tag{3.26}$$

where $\hat{\mathbf{A}}$ is the estimate of $\mathbf{A}$ matrix and the + designates the pseudo-inverse of a matrix. Once the coefficients of the AR model are estimated from Eq. 3.26, the discrete poles of the system can be determined as the eigenvalues of the corresponding companion matrix.

3.3.3 Modified Least Squares Complex Exponential (LSCE) method

In the turning dynamics model developed in Section. 3.1 the static cutting forces were neglected because they do not cause any dynamic deflections. In practice, due to the presence of run-out in the system, the cutting forces excite harmonic response at the spindle rotating frequency and its integer harmonics. Harmonic components usually dominate the response spectrum and therefore they are identified as undamped poles in TDPR method. If the frequency of the harmonic components is well separated from the frequency of the structural modes of the system, one can simply neglect the modes with near zero damping at the harmonics of spindle rotation frequency, because they represent harmonic components of the response. However, if the frequency of the harmonic component is close to the frequency of the structural mode, the undamped nature of the harmonic response greatly affects the accuracy of the identification of the damped poles of the system. To address this issue, Mohanty et al. [35] presented the modified Least Squares Complex Exponential method in which the known harmonic frequencies are included in the identification algorithm as undamped poles. The details of the identification method are available in [35], and a brief description of the method is also provided here.

The discrete poles of the system, μ_p, satisfy the characteristic polynomial of the lumped system in Eq. 3.7:

$$\beta_0 + \beta_1\mu_p^1 + \beta_2\mu_p^2 + \cdots + \beta_{2P-1}\mu_p^{2P-1} + \mu_p^{2P} = 0 \tag{3.27}$$

where $\beta_0, \beta_1, ..., \beta_{2P}$, are the constant coefficients of the characteristic polynomial. One can show that the CF with respect to a single reference also satisfies the characteristic polynomial[33]:

$$\beta_0 + \beta_1 \mathrm{r}_y\left(i\right) + \beta_2 \mathrm{r}_y\left(i+1\right) + \cdots + \beta_{2P-1} \mathrm{r}_y\left(i+2P-1\right) = -\mathrm{r}_y\left(i+2P\right) \quad (3.28)$$

where $\mathrm{r}_y\left(n+1\right)$ is the column of the CF matrix $\mathbf{R}_y$ corresponding to the reference DOF. The harmonic components of the response can be treated as undamped poles that also satisfy the characteristic polynomial (Eq. 3.27). Repeating Eq. 3.28 for np consecutive time steps, and combining the resulting equations with the ones obtained by substituting the undamped poles in the characteristic polynomial, leads to the following system of algebraic equations:

$$\mathbf{E_1 b_1} + \mathbf{E_2 b}_2 = \mathbf{f_1} \quad (3.29)$$

and

$$\mathbf{E_3 b_1} + \mathbf{E_4 b}_2 = \mathbf{f_2} \quad (3.30)$$

where $\left[\begin{array}{ccc} \beta_0 & \cdots & \beta_{2P-1} \end{array}\right] = \left[\mathbf{b}_1{}^T, \mathbf{b}_2{}^T\right]$ and the components of $\mathbf{E_{1,2,3,4}}$ and $\mathbf{f_{1,2}}$ are discrete time CF values and discrete sinusoidal functions of the harmonic terms. The components of these matrices are provided below. In the expanded form, m harmonic frequencies in the signal within the range of frequencies are considered[35].

$$
\begin{aligned}
\mathbf{E_1} &= \begin{bmatrix} \mathbf{r_y}(0) & \cdots & \mathbf{r_y}(2m-1) \\ \vdots & \cdots & \vdots \\ \mathbf{r_y}(np-1) & \cdots & \mathbf{r_y}(np+2m-2) \end{bmatrix} \\
\mathbf{E_2} &= \begin{bmatrix} \mathbf{r_y}(2m) & \cdots & \mathbf{r_y}(2P-1) \\ \vdots & \cdots & \vdots \\ \mathbf{r_y}(np+2m-1) & \cdots & \mathbf{r_y}(np+2P-2) \end{bmatrix} \\
\mathbf{E_3} &= \begin{bmatrix} 0 & \cdots & sin(\omega_1(2m-1)t_s) \\ 1 & \cdots & cos(\omega_1(2m-1)t_s) \\ \vdots & \cdots & \vdots \\ 0 & \cdots & sin(\omega_m(2m-1)t_s) \\ 1 & \cdots & cos(\omega_m(2m-1)t_s) \end{bmatrix} \\
\mathbf{E_4} &= \begin{bmatrix} sin(\omega_1 2mt_s) & \cdots & sin(\omega_1(2P-1)t_s) \\ cos(\omega_1 2mt_s) & \cdots & cos(\omega_1(2P-1)t_s) \\ \vdots & \cdots & \vdots \\ sin(\omega_m 2mt_s) & \cdots & sin(\omega_m(2P-1)t_s) \\ cos(\omega_m 2mt_s) & \cdots & cos(\omega_m(2P-1)t_s) \end{bmatrix} \\
\mathbf{f_1} &= \begin{bmatrix} \mathbf{r_y}(2P) \\ \vdots \\ \mathbf{r_y}(np+2P-1) \end{bmatrix} ; \mathbf{f_2} == \begin{bmatrix} sin(\omega_1 2Pt_s) \\ cos(\omega_1 2Pt_s) \\ \vdots \\ sin(\omega_m 2Pt_s) \\ cos(\omega_m 2Pt_s \end{bmatrix}
\end{aligned}
\tag{3.31}
$$

While Eq. 3.29 enforces Eq. 3.28 at a set of time steps, Eq. 3.30 enforces the harmonic terms to be undamped poles of the system. Therefore, in order to guarantee that the harmonic terms are included as undamped poles, Eq.3.30 must be exactly satisfied. The exact solution of Eq. 3.30 leads to the following:

$$\mathbf{b_1} = \mathbf{E_3}^{-1}\left[\mathbf{f_2} - \mathbf{E_4}\mathbf{b}_2\right] \tag{3.32}$$

Substituting Eq. 3.33 in Eq. 3.29 results in the following overdetermined system of equations:

$$\left(\mathbf{E_2} - \mathbf{E_1}\mathbf{E_3}^{-1}\mathbf{E_4}\right)\mathbf{b}_2 = \mathbf{f_1} - \mathbf{E_1}\mathbf{E_3}^{-1}\mathbf{f_2} \tag{3.33}$$

The least squares approximation of $\mathbf{b_2}$ can be obtained from Eq. 3.33, and along with the corresponding solution of $\mathbf{b_1}$ obtained from Eq. 3.32 will form the complete solution of the coefficients of the characteristic polynomial, $\beta_0, ..., \beta_{2P-1}$. Poles of the system are then obtained as the roots of the characteristic polynomial. Note that the $2P$ roots of the polynomial include the considered harmonic terms and the damped structural modes of the system as pairs of complex conjugate poles.

Chapter 4

Simulations and Results[1]

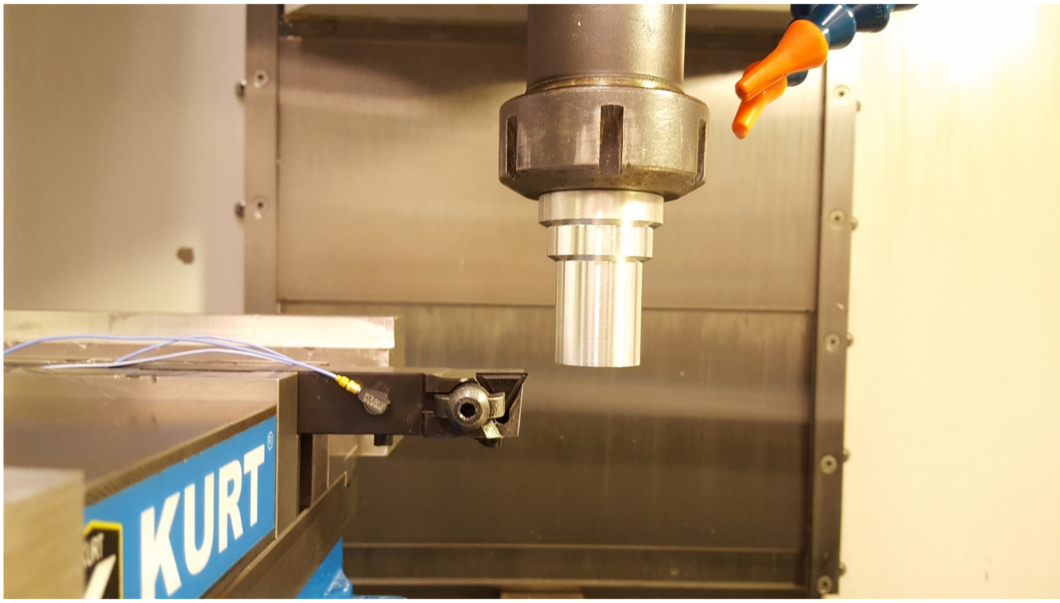

Figure 4.1: The test setup of orthogonal turning experiments

The experimental setup used in this work is shown in Fig. 4.1. A turning tool holder with 38 mm overhang length and 19X19 mm^2 cross section is mounted on the table of a CNC milling machine. A cylindrical workpiece with 38 mm diameter and 51 mm overhang is mounted on the spindle. A triangular turning insert with zero degrees rake and approach angles is used to machine the workpiece in the axial direction using 0.05 mm/rev feedrate and various spindle speeds and width of cuts. Two PCB accelerometers are

---

[1] This chapter is under review for journal publication April 15, 2019

installed on the tool in each of the feed (z) and normal (y) direction at the positions indicated in Fig. 4.1 and Fig. 3.1. In each direction, one of the accelerometers is installed close to the tooltip and the other one at 25 mm from the tooltip. A four-channel National Instrument Data Acquisition (DAQ) card was used to digitize the accelerometer signals at 16384 Hz sampling rate. The digitized signals were stored on a personal computer. Also, a unidirectional microphone is placed near the tool to record the sound pressure during machining. The direct and Frequency Response Functions (FRFs) between all four degrees of freedom measured using an impulse hammer test are shown in Fig. 4.2. Modal Analysis was performed in Cutpro software to identify the mass-normalized mode shapes, natural frequencies, and modal damping ratios of the two dominant modes at 1842 and 2445 Hz. The modal parameters of these two modes are shown in Table 4.1, and the FRFs that are constructed using the identified two modes are superimposed on the measured FRFs in Fig. 4.2. The two modes shown in Table 4.1 are used to obtain the stability

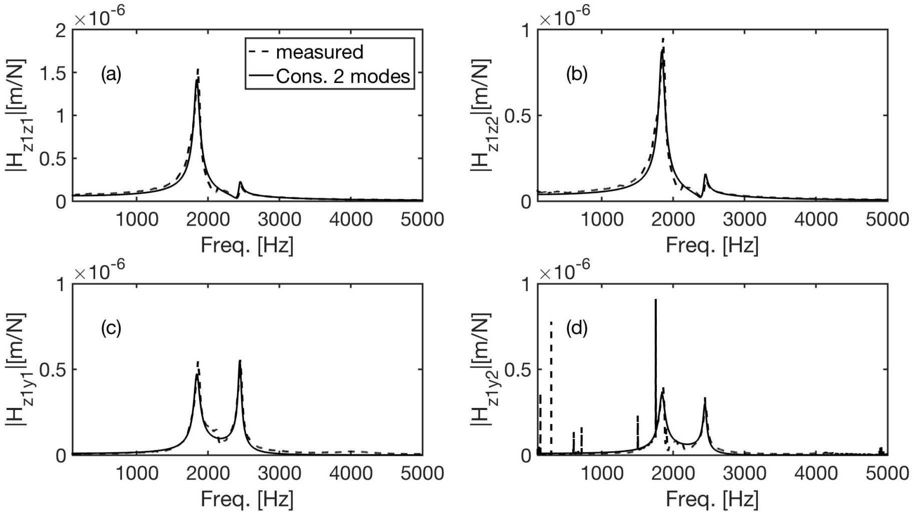

Figure 4.2: Direct and cross FRFs between the four DOFs (z_1, z_2, y_1, y_2) of the turning tool

diagrams of the system. The stability diagrams can be obtained by setting up a grid of spindle speed and width of cut values and determining the stability of vibrations at each point of the grid according to the largest eigenvalue of the transition matrix in Eq. 3.7. The stability diagrams also can be obtained analytically by directly employing the FRFs in the frequency domain solution

Table 4.1: Modal parameters of the dominant modes of the turning setup

Mode	Frequency [Hz]	Damping ratio [%]	Mode shape $[z_1, z_2, y_1, y_2]^T$
1	1842	0.021	$[2.81, 1.73, -0.94, -0.71]^T$
2	2445	0.009	$[0.92, 0.66, 2.55, 1.39]^T$

of the DDE as presented in [3]. The frequency domain solution was used in this paper and the resulting stability diagrams are shown in Fig. 4.3

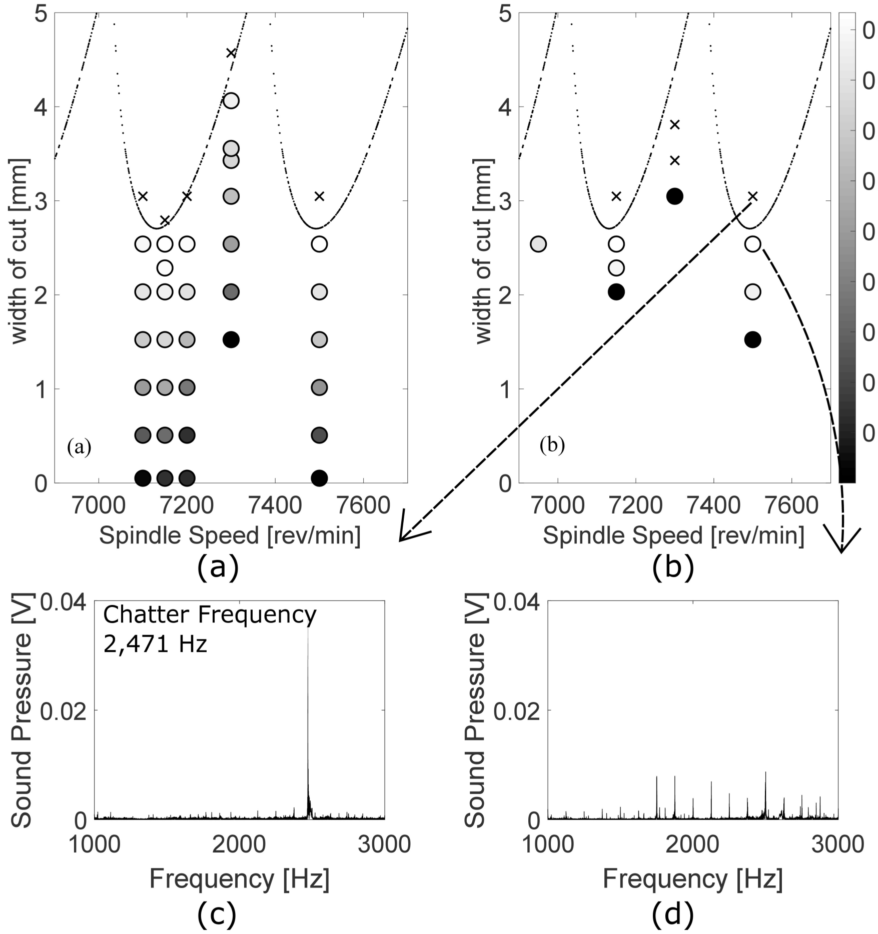

(a) (b)

(c) (d)

Figure 4.3: Stability diagrams of the turning system, and the damping ratio of the system identified from vibration signals obtained from numerical simulations(a), and from the vibration signals measured during turning operations (b); Frequency Spectrum of the sound signals recorded during turning at (c) 7500 rev/min spindle speed and 3.05 mm depth of cut, (d) 7500 rev/min and 2.54 mm depth of cut

4.1 Numerical Simulations

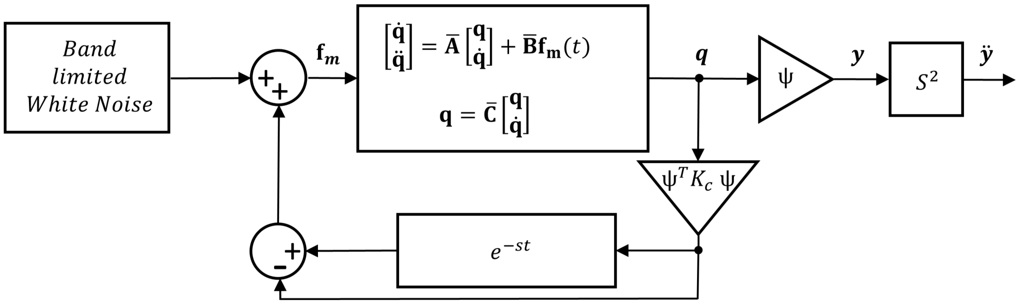

Figure 4.4: Block Diagram of the numerical simulations of self-excited vibrations during turning

The block diagram shown in Fig. 4.4 outlines the algorithm used to numerically simulate the accelerations at the four measurement DOFs of the tool when arbitrary spindle speed and depth of cuts are used. The tool dynamics is represented by the two modes shown in Table 4.1. Assuming proportional damping, the mass-normalized mode shape vectors (Ψ_1 and Ψ_2) in Table 4.1 are used to convert the equation of motion of the tool from the physical space in Eq. 3.1 to modal space:

$$\begin{aligned}
&\ddot{\mathbf{q}} + \mathbf{c}_m\dot{\mathbf{q}} + \mathbf{K}_m\mathbf{q} = \mathbf{f}_m(t);\\
&\mathbf{y} = [\boldsymbol{\Psi_1} \quad \boldsymbol{\Psi_2}]\mathbf{q}\\
&\mathbf{C}_m = diag(2\xi_1\omega_1, 2\xi_2\omega_2)\\
&\mathbf{K}_m = diag((2\pi f_1)^2, (2\pi f_2)^2)\\
&\mathbf{f}_m(t) = [\Psi_1 \quad \Psi_2]^T\mathbf{f}_t
\end{aligned} \tag{4.1}$$

where $\mathbf{q}$ is the modal displacement vector. The following state space form of Eq. 4.1 is used in the numerical simulations:

$$\begin{aligned}
&[\dot{\mathbf{q}} \quad \ddot{\mathbf{q}}]^T = \bar{\mathbf{A}}[\mathbf{q} \quad \dot{\mathbf{q}}]^T + \bar{\mathbf{B}}\mathbf{f}_m(t)\\
&q = \bar{\mathbf{C}}[\mathbf{q} \quad \dot{\mathbf{q}}]^T
\end{aligned} \tag{4.2}$$

where $\bar{\mathbf{A}}$, $\bar{\mathbf{B}}$ and $\bar{\mathbf{C}}$ are the system matrices in modal space:

$$\begin{aligned}&\bar{\mathbf{A}} = \left[\begin{array}{cc} 0 & \mathbf{I} \\ -\mathbf{K_m} & -\mathbf{C_m} \end{array}\right], \bar{\mathbf{B}} = \left[\begin{array}{c} 0 \\ \mathbf{I} \end{array}\right], \bar{\mathbf{C}} = \left[\begin{array}{cc} \mathbf{I} & 0 \end{array}\right]; \\ &\mathbf{I} = \mathbf{I_{2X2}}, \quad \mathbf{0} = \mathbf{0_{2X2}}\end{aligned} \tag{4.3}$$

The cutting force coefficients of the Al 6061 workpiece are obtained using orthogonal to oblique transformation method [3] at $K_t = 635$ and $k_f = 159$ MPa. The closed loop system shown in Fig. 4.4 is assumed to be initially at rest, and it is excited by normally distributed white noise at every 0.01 ms simulation time step. The resulting accelerations at the four DOFs are obtained by numerically integrating the modal state space equation (Eq. 4.2). The system response is simulated for 10 seconds, and each simulation is repeated two times to obtain two data sets. The data set obtained from the first simulation is used for the identification of the system poles, and the data set from the second simulation is used for the cross-validation of the model identified using the first data set. For example, Fig. 4.5 shows the Singular Values of the PSD matrices of the responses used for the identification (data set 1) of the system poles when the spindle speed and with of cut are respectively (a) 7500 rev/min and 2.03 mm, (b) 7500 rev/min and 2.54 mm, (c) 7300 rev/min and 3.05 mm, and (d) 7300 rev/min and 4.06 mm. According to the stability diagrams shown in Fig. 4.3, at 7300 rev/min the system has the lowest stable depth of cut and at 7300 rev/min coincides with one of the stability pockets of the system. Only the first two (out of four) singular values of the responses are shown in Fig. 4.5, because the smallest two singular values are below -100 dB. The CF of the simulated acceleration signals is computed at $np =$ 1500 time steps using direct method[6]. The resulting CF is then used in the TDPR identification method discussed in Section 3.3.2 to identify the modal frequency and damping ratio of the dominant poles of the system.

In order to determine the suitable AR model order, na, stabilization diagrams and cross-validation methods are used. The stabilization diagram of each simulated case is obtained by increasing the model order from $na = 2$, at unit increments, to $na = 40$. After each model order increment, the frequencies and damping ratios of the identified poles are compared with their corresponding values at the preceding model order, and the poles with a positive damping

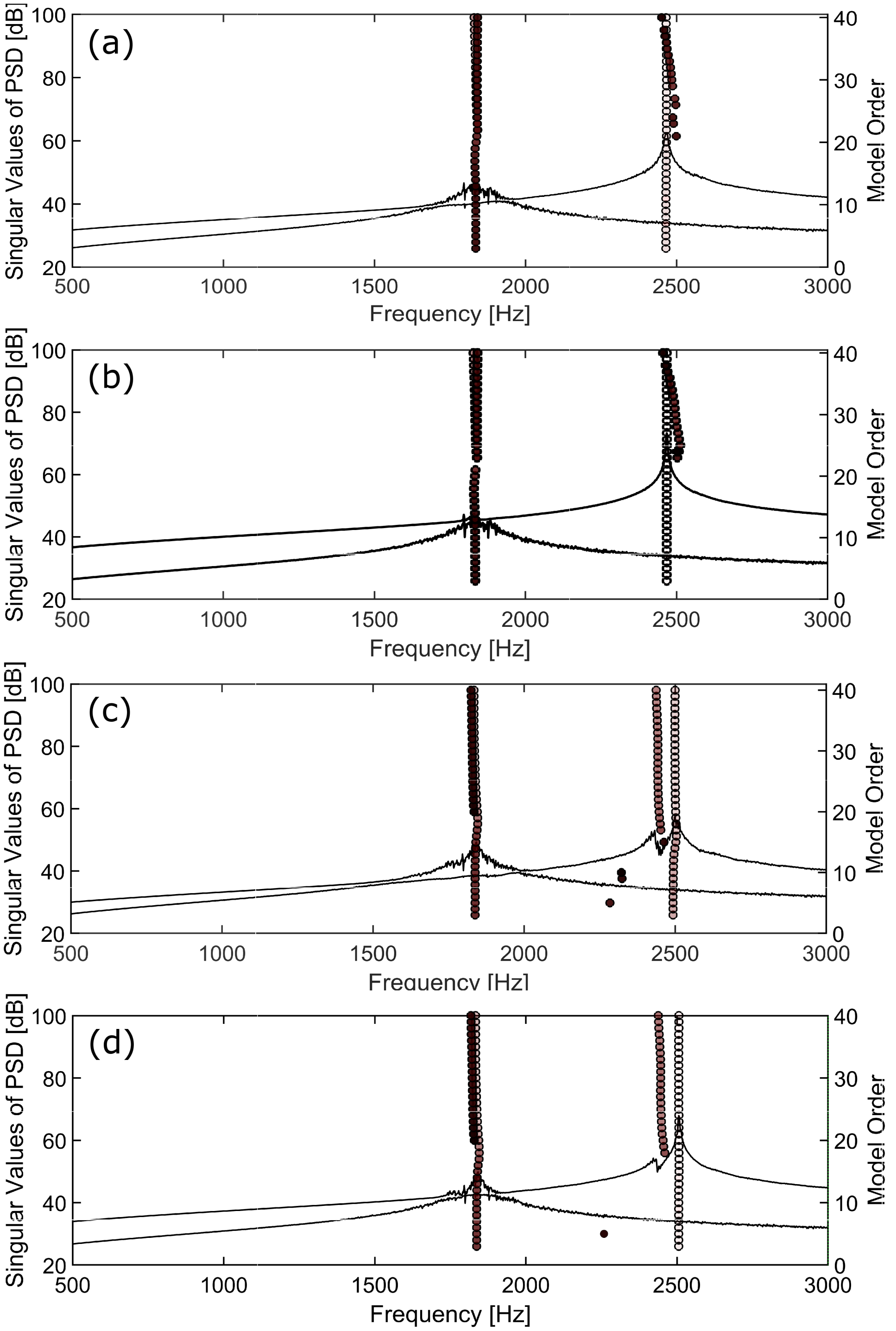

Figure 4.5: Stabilization diagrams of the TDPR identification performed on the vibration signals obtained from numerical simulations of the turning process at (a) 7500 rev/min and 2.03mm depth of cut, (b) 7500 rev/min and 2.54mm depth of cut, (c) 7300 rev/min and 3.05 mm depth of cut, and (d) 7300 rev/min and 4.06 mm depth of cut.

ratio that vary less than 0.2 % in their frequency are identified as stable modes and shown with a circle on the PSD diagrams. Therefore, a streak of circles on the stabilization diagram indicates an identified system pole. The shading of the circles are proportional to their damping ratio. Darker circles are the poles with a higher damping ratio and the light circles have a lower damping ratio.

The stabilization diagram of the simulated vibrations at 7500 rev/min spindle speed and 2.03 mm width of cut is shown in part (a) of Fig. 4.5. At this point, two stable modes are identified, a highly damped mode at 1832 Hz and a lightly damped mode at 2465 Hz, the former originating from mode 1 in Table 4.1 and the latter originating from mode 2. When the width of cut increases to 2.54 mm at the same spindle speed (7500 rev/min), as shown in the part (b) of the figure, two stable modes are identified at 1835 Hz with a high damping (indicated by dark circles) and 2468 Hz with very low damping (nearly blank circles). By increasing the width of cut to 3.05 mm at 7500 rev/min, the vibration signals become unstable and therefore identification of the modes using TDPR method becomes impossible. Unstable points are indicated by crosses in Fig. 4.3 (a). At 7300 rev/min, the second mode of vibration at 2445 Hz synchronizes with the spindle frequency (2445 Hz = 20×121.7 Hz), producing twenty complete waves in every revolution. Because of the synchronization of the spindle revolution frequency and the vibration frequency, a higher stability limit is obtained at this speed causing the stability pocket in the stability diagram shown in Fig. 4.3. As shown in parts (c) and (d) of Fig. 4.5, the PSD of simulated signals at 7300 rev/min include two closely spaced peaks at around the second mode of vibrations (2445 Hz). The TDPR identification method identifies the frequencies and damping ratios of both of the peaks around the second mode as well as the frequency and damping of the peaks around the first mode. In both cases, 3.05 mm depth of cut in part (c) and 4.06 mm in part (d), each mode is split into a lightly damped mode with higher participation (converges at lower model order) and a mode with higher damping and lower participation. At 3.05 mm width of cut, the mode with the smallest damping ratio is at 2499 Hz; at 4.06 mm, the mode with the lowest damping ratio is at 2506 Hz. Clearly, the lowest damping ratio reduces by increasing the width of the cut from 3.05 to 4.06 mm. At 4.32 mm width of cut, the tool vibrations become unstable in agreement with the stability diagrams. The overall reduction of the damping ratios of the identified modes

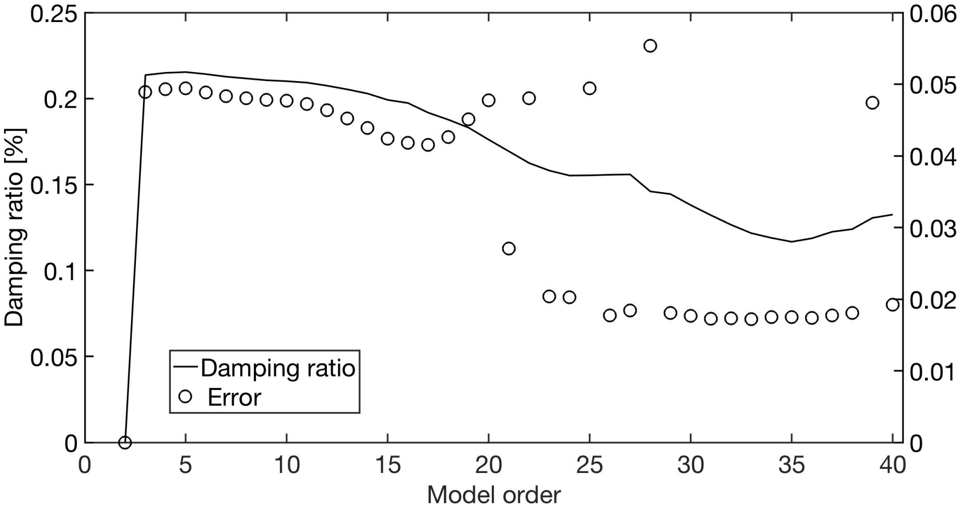

Figure 4.6: Estimation error and damping ratio of the dominant pole obtained from TDPR identification using the AR models with various orders; vibration signals are obtained from the simulation of the turning process at 7500 rev/min and 2.03 mm depth of cut

when the width of cut approaches the stability limit is clear in Fig. 4.5 and a similar trend is observed in simulations at other spindle speeds. As also shown in the stabilization diagrams in Fig. 4.5, the frequencies of the stable modes do not change significantly ($< 0.2\%$) by changing the order of the AR model used to approximate the CF. However, unlike the frequencies, the damping ratio of the identified modes vary by changing the model order. For instance, the damping ratio of the second mode in Fig. 4.5(a) when various model orders are used in shown in Fig. 4.6. Also shown in this figure is the resulting estimation errors when models with various orders are used. In order to obtain the estimation error, the identified poles ($\hat{\mu}_p$) are employed in Eq. 3.16 to reconstruct the CF of the vibration signals in the second dataset:

$$\mathbf{R}_y(i) = \sum_{p=1}^{2P} \mathbf{B}_p \mu_p^i \tag{4.4}$$

Note that $\mathbf{R}_y$ in Eq. 4.4 are the CF of the vibration signals in the second dataset, and P is the number of identified stable modes. For example, in Fig. 4.5(a) to estimate the error when $na = 10$, only two stable modes are included and therefore $P = 2$. Unknown constant matrices, $\mathbf{B_p}$, are composed of deflection shapes associated with the pole number p. These unknown matrices are determined by repeating Eq. 4.4 for the first i= 0...np time steps and then using the following Least Squares approximation:

$$\begin{gathered}[\hat{\mathbf{B}}_p \quad \cdots \quad \hat{\mathbf{B}}_{2P}]^T = \mathbf{Z}^{+}[\mathbf{R_y(0)} \quad \cdots \quad \mathbf{R_y(np)}]^{\mathbf{T}} \\ \mathbf{Z} = \begin{bmatrix} \hat{\mu}_1^0 & \hat{\mu}_2^0 & \cdots & \hat{\mu}_{2P}^0 \\ \hat{\mu}_1^1 & \hat{\mu}_2^1 & \cdots & \hat{\mu}_{2P}^1 \\ \vdots & \vdots & \vdots & \vdots \\ \hat{\mu}_1^{np} & \hat{\mu}_2^{np} & \cdots & \hat{\mu}_{2P}^{np} \end{bmatrix}\end{gathered} \tag{4.5}$$

where $\hat{\mathbf{B}}_p$ stands for the least square approximation of $\mathbf{B_p}$. Reconstructed CF, $\hat{\mathbf{R}}_y(i)$ are obtained by replacing $\mathbf{B}_p$ in Eq. 3.16 by its approximation $\hat{\mathbf{B}}_p$:

$$\hat{\mathbf{R}}_y(i) = \sum_{p=1}^{2P} \hat{\mathbf{B}}_p \hat{\mu}_p^i \tag{4.6}$$

The estimation error at each time step is defined as the Euclidean norm of the difference between the reconstructed and measured (simulated) CF:

$$\epsilon(i) = \parallel \hat{\mathbf{R}}_y(i) - \mathbf{R}_y(i) \parallel \tag{4.7}$$

The norm of the estimation error (ϵ) at 7500 rev/min and 2.03 mm is shown in Fig. 4.6. According to this figure, the estimation error is minimum when the

Table 4.2: Modes obtained from TDPR identification of vibration signals simulated at 7500 rev/min spindle speed as the depth of cut increases from zero to the stability limit

	Mode 1		Mode 2	
a[mm]	Frequency [Hz]	Damping [%]	Frequency [Hz]	Damping [%]
0	1845	2.16	2455	0.98
0.508	1845	2.16	2455	0.98
1.016	1843	2.1	2463	0.52
1.524	1842	2.03	2465	0.3
2.032	1841	1.95	2466	0.16
2.54	1840	1.84	2468	0.04

AR model with order $na = 25$ is used. At this model order, the damping ratio of the second mode at 2466 Hz is estimated at 0.16 % ($\xi_2 = 0{:}0016$). Similar cross-validation method is used to determine the optimum model order and the corresponding damping ratio in all of the other simulated cases.

The frequency and damping ratio of the poles identified from the simulated vibrations at 7500 rev/min and depth of cut $0 < a < 2.54$ mm are shown in Table 4.2. A similar analysis is performed at a set of spindle speed and depth of cut values and the results are demonstrated in Fig. 4.5(a). Simulation at each spindle speed and width of cut that results in stable vibrations is represented with a circle in Fig. 4.3; simulations at points that result in unstable vibrations are shown with a cross. At each simulation point, the shading of the corresponding circle is proportional to the lowest identified damping ratio at that point. As seen in this figure, at all of the spindle speeds, as the width of cut approaches the stability limit, the damping ratio approaches zero. The variation of the smallest damping ratio and the corresponding modal frequency as the width of varies between zero and 2.54 mm at 7500 rev/min is shown in Fig. 4.7. As shown in this figure, when the width of cut is small, the damping ratio approaches the modal damping of the tool's second mode (2445 Hz, and 0.09 % damping). As the width of cut approaches the stability limit, the damping ratio decreases to 0.06 % and the frequency increases to 2468 Hz.

4.2 Signal Processing

Four accelerometers measure vibration at the tool in Figs. 3.1 and 4.1 at the same time, machining sound is recorded to verify chatter during orthogonal turning operation using the Haas CNC machine.

The signals from sensors during the turning operation are blue plots and the steady state signals collected to conduct data processing are black in Fig. 4.8 (a). To obtain the Power Spectral Density (PSD) shown in Fig. 4.8 (b), (c) and (d), the CFs are computed using direct method[11] from the steady states signal shown in black at (a). Then, sampling time step Δt is $5.86e-05sec$ and the number of data points in the data segments or window size (np) is 900. Note that the PSD does not play a role in the analysis process, but it is required to gain an initial estimation of the dominant frequencies through the

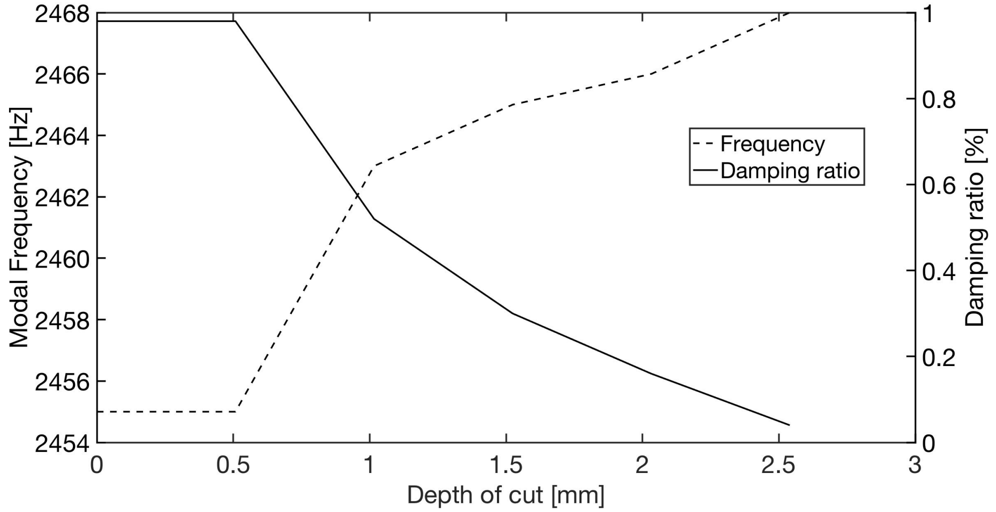

Figure 4.7: Frequency and damping of the dominant mode obtained from the TDPR identification of the vibrations simulated at 7500 rpm and various depth of cuts.

measured vibrations. Furthermore, later, CF verifies the accuracy of the analysis results using the reconstructed CF by comparing the original themselves. As shown in the PSD plot in Fig. 4.8 (b), (c) and (d), harmonic frequencies of spindle appears as an integer multiple of 125 Hz from 7500 rpm spindle speed on the green vertical lines. They are seen clearly in the frequency domain from 1600 Hz to 3000 Hz. The modes in the tests of 2.03 mm and 2.54 mm width of cut are located at between 19^{th} multiple, 2375 Hz, and 20^{th} multiple, 2500 Hz spindle harmonics. However, in the case of 1.02 mm width of cut in Fig. 4.8 (b), the mode has not been found due to high stability with a small depth of cut machining. The mode at the 2.03 mm of a width of cut with 0.051 mm/rev feed rate in 7500 rpm turning process shown in Fig. 4.8 (c) is located at the 2475 Hz and the mode at the 2.54 mm width of cut shown in Fig. 4.8 (d) is clearer and the peak is noticeably higher than other modal frequencies compared to the results of another width of cut.

Aforementioned, the reconstructed CF employing the identified modal frequencies and damping ratios in the least-squares equation is compared in Fig. 4.9 and 4.10. The CF using the direct method[11] from the measured signal of experiments is red dash lines and its reconstructed CF from the result of the modified LSCE method is blue lines. The CF is composed of two signals

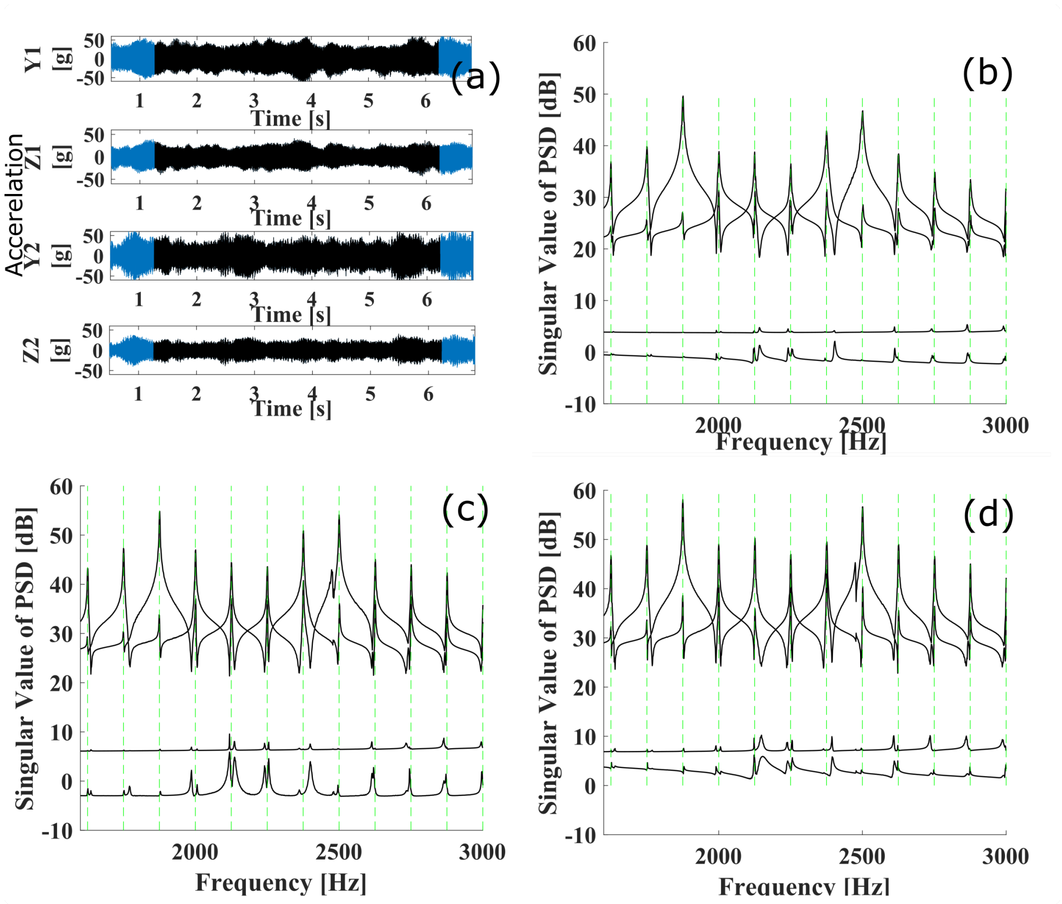

Figure 4.8: Measured signal (a) at 2.03 mm width of cut and the PSD, frequency range 1,600 Hz to 3,000 Hz, of 1.02 mm width of cut (b), 2.03 mm width of cut (c) and 2.54 mm width of cut (d) at 0.051 mm/rev feed rate in orthogonal turning at 7,500 rpm spindle speed.

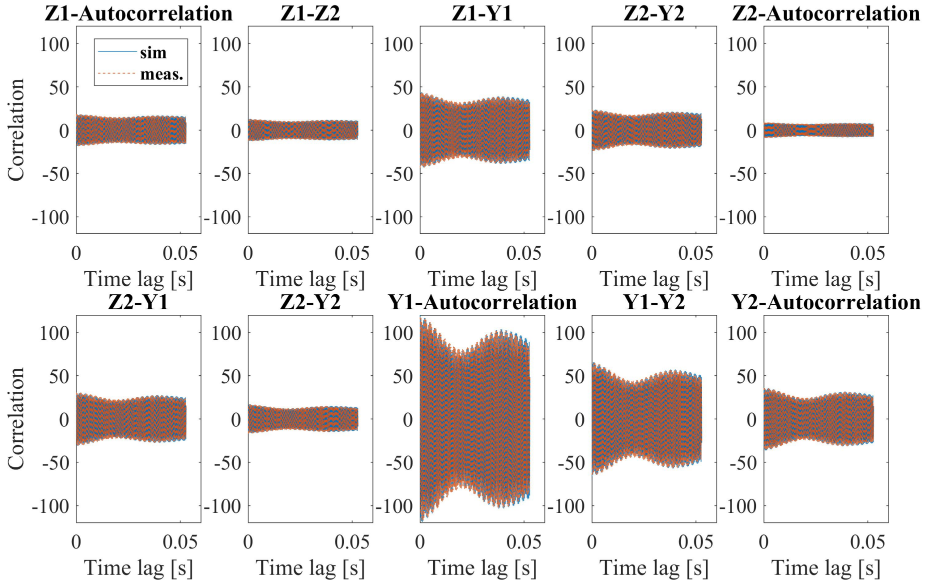

Figure 4.9: CF (red) and reconstruct CF (blue) at 2474 Hz at a 7500 rpm spindle speed , a 2.03 mm width of cut and 0.051 mm/rev feed rate in orthogonal turning.

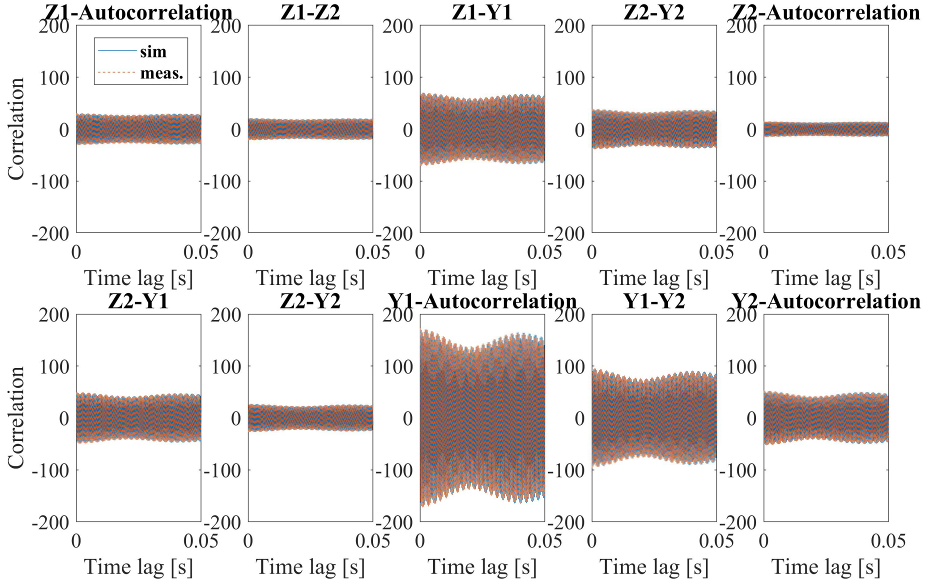

Figure 4.10: CF (red) and reconstruct CF (blue) at 2474 Hz at a 7500 rpm spindle speed , a 2.54 mm width of cut and 0.051 mm/rev feed rate in orthogonal turning.

or own signal from a certain sensor and shows correlation or autocorrelation respectively. In the experiment, four sensors, two in the feed direction and the

others in cutting direction, were used to measure the signal, and two signals are paired to form a correlation function. In this case, since a single signal produces an autocorrelation function, a total of ten individual correlation functions are obtained. Note that, CFs in this section are shown to validate the accuracy of the experiment using OMA techniques.
In the turning process at the constant feed speed, the vibration in the cutting direction is larger than the vibration in the feed direction due to the physical characteristics of the rotating structure and the machining method where workpiece and a tool are perpendiculars. It also measures vibrations with a greater amplitude as the position of the sensor is closer to the machining point or farther away from the tool holder. For this reason, in each experiment, the autocorrelation function of Y1 has the largest amplitude and is shown in Fig. 4.9 and 4.10. In Fig. 4.9 and 4.10, red dash lines are CF of the measured signal and the blue lines indicate reconstructed CF of the result of the modified LSCE method. The reconstructed CF corresponds to the CF made of the measured signal in both 2.03 mm and 2.54 mm width of cut in orthogonal turning tests. Fig. 4.9 at the 2.03 mm width of cut shows greater decay rather than Fig. 4.10 at 2.54 mm width of cut. From this, the more damping in a smaller width of cut is estimated. The amplitude of vibration at 2.54 mm width of cut is significantly greater known from the Figs 4.9 and 4.10.

4.3 Experimental Results

The singular values of the PSD of the measured acceleration signals at 7500 rev/min and 2.05 mm width of cut is shown in Fig. 4.11. Only the two largest singular values are shown because the two smallest singular values are below -100 dB. The integer harmonic of the spindle revolution frequency (125 Hz) are indicated by green vertical lines. As shown in this figure, sharp peaks are observed at the harmonics of the spindle frequency due to the strong presence of harmonic excitation. Also, a peak is observed next to the 20^{th} harmonic of the spindle, which indicates the structural mode of vibration. No peaks observed near the first mode at 1842 Hz, because this mode has higher damping and is suppressed by the harmonic terms that have virtually zero damping and a high participation in the response. Before applying TDPR identification method on the measured response, the average term of the frequency spectrum of the acceleration signals is removed by applying de-trending FFT filter[11]. Also, unlike the simulated data (in Section 4.1), as shown in Fig. 4.11, the measured signals include many structural modes and harmonic components that require a very high order AR model. In order to avoid requiring a high order AR model (which might cause numerical errors), a bandpass FFT filter is applied around the observed structural mode (around 2476 Hz). The flat range of the bandpass filter is 0.25 % of the spindle frequency and the total width of the pass band of the filter is 0.75 % of the spindle frequency. The CF of the filtered signals are computed using direct method [11] and used in the TDPR method to identify the poles of the system within the pass band of the bandpass filter. The resulting stabilization diagram of the identification at 7500 rev/min and 2.05 mm width of cut is shown in Fig. 4.11(a). Similar to the method used in Section 4.1, the stabilization diagram was developed by increasing the model order at unit increments. The identified poles at each increment are considered stable and indicated by a circle in the stabilization diagram if their frequency is within 0.2 % of their corresponding frequency in the previous model order. The color shading of the circle is proportional to their corresponding modal damping ratio. Darker circles indicate higher damping. As shown in Fig. 4.11 (a), the harmonic response peak at 2500 Hz is identified as a pole with near zero damping, but the structural mode next to the harmonic mode does not converge to a stable frequency. Although TDPR method efficiently identified the poles of the system in numerical simulations where the harmonic component of the response was neglected, it is not effective in identifying the modes from experimentally measured signals due to the strong presence of harmonic components.

To compensate for the undamped effect of the harmonic components in the computed CF, the modified LSCE method explained in Section 3.3.3 is used. Three harmonic terms at 19, 20, and 21 times the spindle frequency are considered as undamped poles of the system in the CF computed using the direct method with respect to z_1 DOF. The resulting stabilization diagram at 7500 rev/min and 2.05 mm width of cut is shown in part (b) of Fig. 4.11. Using the modified LSCE method, the three harmonic terms are identified as poles with zero damping and the structural mode is identified at 2476 Hz. Similar to the numerical simulation in Section 4.1, , and L-curve method is used to determine the suitable model order, except that in this section the CF with

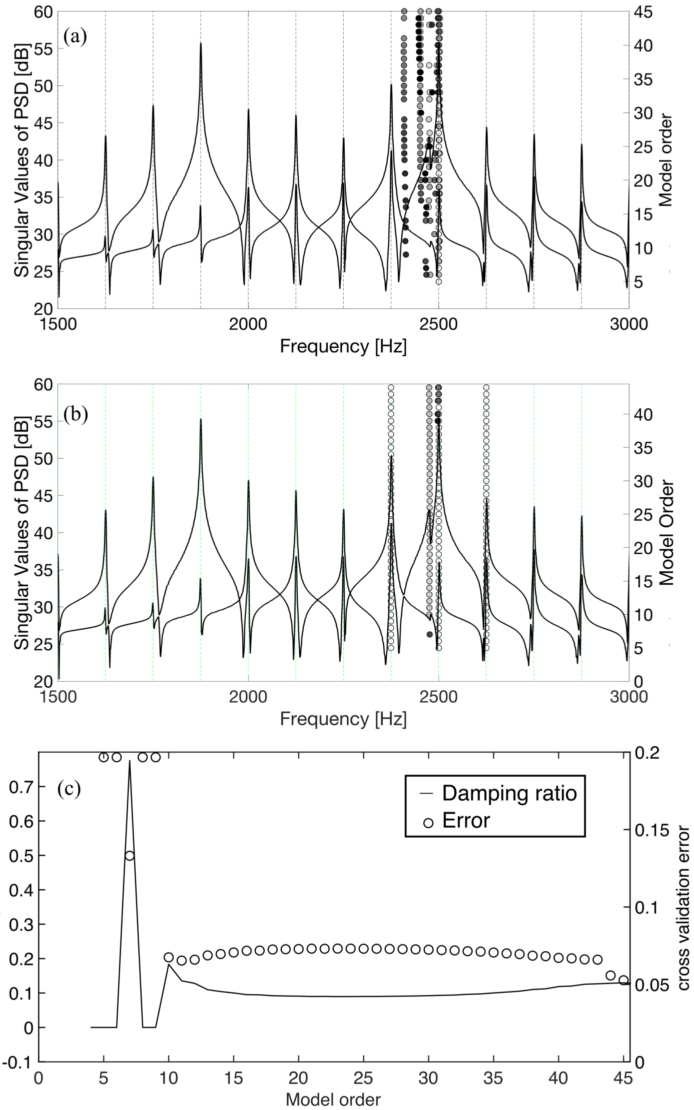

Figure 4.11: (a) Stabilization diagram of TDPR identification performed on the vibration signals measured at 7500 rev/min and 2.03 mm depth of cut, (b) Stabilization diagram of modified LSCE identification performed on vibrations measured at 7500 rev/min and 2.03 mm depth of cut, and (c) the estimation error and the damping ratio of the dominant mode identified from the AR model (with various orders) of the turning system at 7500 rev/min and 2.03 mm depth of cut

respect to y_1 DOF is used for cross-validation. The resulting estimation error at each model order is shown in part (c) of Fig. 4.11. The estimation error is minimum at $n = 11$ and therefore this number is used as the optimum model order. The corresponding damping ratio of the pole at 2476 Hz is estimated at 0.13 %. Variation of the estimated damping ratio at various model orders is also shown in Fig. 4.11 (c).

The PSD of the acceleration signals measured at (a) 7500 rev/min and 2.54 rev/min, (b) 7300 rev/min and 3.05 mm, (c) at 7150 rev/min and 2.03 mm, and (d) 7150 rev/min and 2.54 mm are shown in Fig. 4.12. Similar to Fig. 4.11, detrending, and bandpass filters around the observed structural modes are applied before the modified LSCE identification method is used to identify the frequency and damping of the structural poles. In part (a) of the figure, the stabilization diagram resulting from identification at 7500 rev/min and 2.54 mm width of cut shows a stable mode at 2477 Hz with 0.066 % damping ($n = 11$ model order). By increasing the width of cut to 3.05 mm at 7500 rev/min the cut becomes unstable, which is also predicted by the stability diagrams in Fig. 4.3. At 7300 rev/min, where the 20^{th} harmonic of the spindle frequency coincides with the second vibration mode, the cut is stable at 3.05 mm but becomes unstable at 3.3 mm width of cut. The higher stability at this spindle speed was also observed in numerical simulations and predicted by stability diagrams, however, the stability limit (3.3 mm) is smaller than the simulation result (4.06 mm). This discrepancy might be due to un-modeled process disturbances. As shown in part (b) of Fig. 4.12, no structural peaks are observed even at the highest stable width of cut (3.05 mm) and therefore system identification cannot be performed when the cut is performed inside one of the stability pockets of the stability diagrams, because the structural mode in these pockets coincides with one of the harmonic components of the signal and therefore cannot be identified. To examine the consistency of the identification results, poles of the system at 7150 rev/min and 2.29 mm and 2.54 mm width of cut are identified and the results are shown in parts (c) and (d) of Fig. 4.12, respectively. As shown in these figures, at 2.29 mm, a stable structural pole is identified at 2474 Hz with 0.12 % damping ratio, and at 2.54 mm damping of this mode reduces to 0.076 % and its frequency increases to 2477 Hz. At 3.05 mm width of cut vibrations become unstable, similar to 7500 rev/min.

A similar analysis is performed at a set of spindle speed and width of cut values examined in experiments and the results are summarized in Fig. 4.3(b). Also, the stability diagrams are duplicated in this figure to enable a comparison between experimental results, analytically obtained stability limits, and numerical simulations presented in part (a) of the figure. The black circles in part (b) of the figure are the points at which the damping ratio of a structural pole was not low enough to overcome the dominance of the harmonic components in its vicinity and therefore no peaks were observed in the PSD and identification was not performed. Because the damping of the structural poles is unknown at these points, the modal damping of the second mode in an idle condition (0.9 %) is assigned. The circles with light shading are the points at which the damping and frequency of the structural mode were successfully identified using modified LSCE method. Darker shading indicates higher damping. Crosses indicate points at which chatter was detected both in the measured vibration signals and the recorded sound pressure. According to Fig. 4.3, the damping ratio and frequency of the structural poles identified from experiments closely agrees with numerical simulations when the width of cut is close enough to the stability borders for the structural mode to appear in the PSD of the response, otherwise the structural mode is suppressed by the harmonic components and cannot be identified. Parts (c) and (d) of Fig. 4.3 show the frequency spectrum of the sound pressure recorded at 7500 rev/min and 2.54 mm (stable point) and at 7500 rev/min and 3.05 mm (unstable point). According to this figure, no peaks close to the frequency of the vibration modes of the system (1842 Hz and 2445 Hz) are detected in the sound signal. When the width of cut crosses the stability limit, a sharp peak appears at 2471 Hz indicating chatter. While the spectrum of sound pressure signal detect chatter after vibrations become unstable, the presented method can be used to monitor the declining trend of the damping of the structural mode to indicate the loss of stability while the cut is still stable.

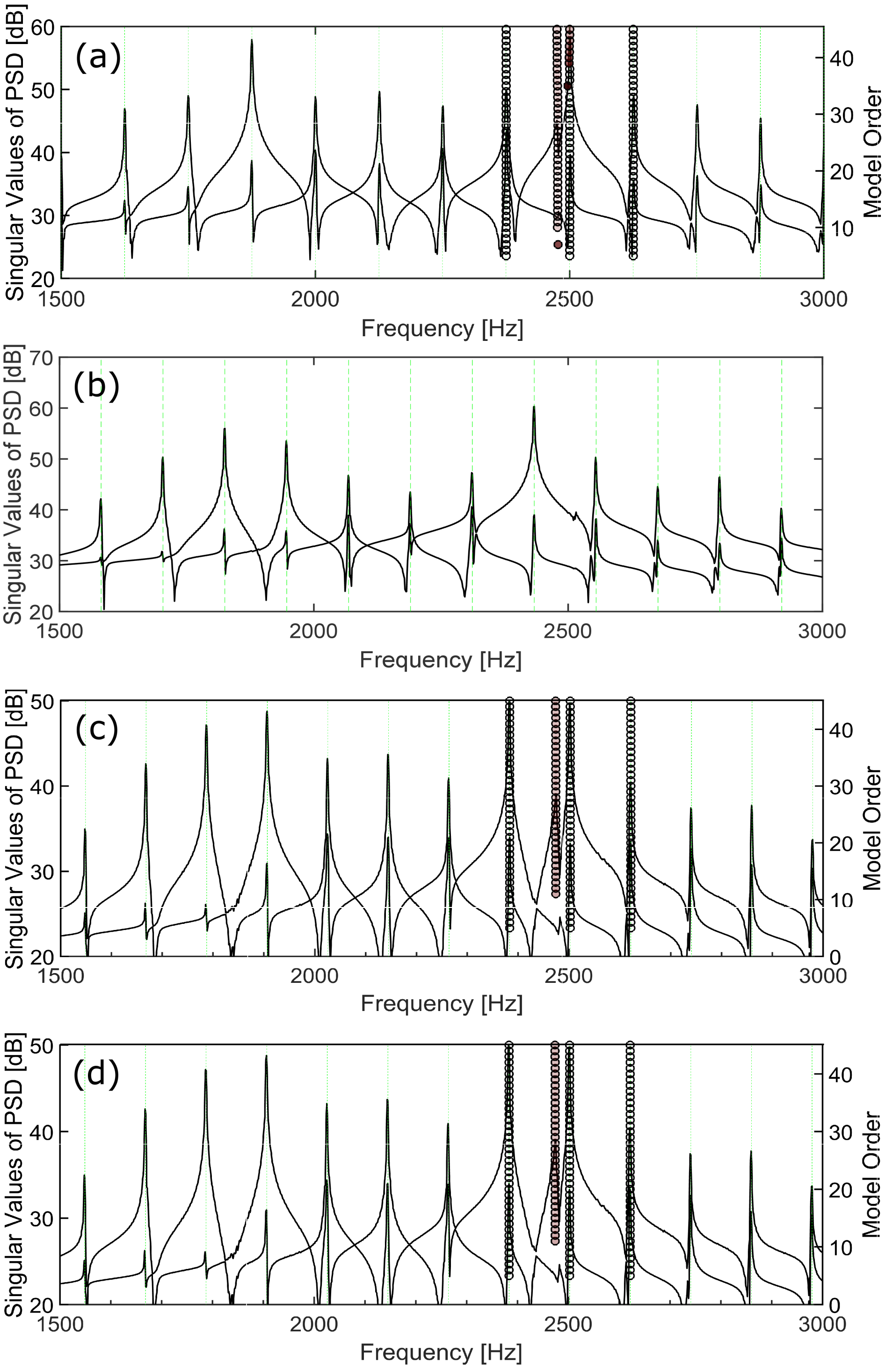

Figure 4.12: Stabilization diagram of modified LSCE identification performed on the vibration signals measured at (a) 7500 rev/min and 3.05 mm depth of cut, (b) 7300 rev/min and 3.05 mm depth of cut, (c) 7150 rev/min and 2.29 mm depth of cut, and (d) 7150 rev/min and 3.05 mm depth of cut

Chapter 5

Summary and Conclusion

Regenerative vibrations in turning processes were modeled using a finite dimensional lumped system in the discrete time domain, and the poles of the resulting system were identified using Operational Modal Analysis of the vibrations measured during the process. The presented method was used to identify the damping ratio of the dominant poles of the turning system, which decrease as the system moves towards the border of stability. The variation of the damping ratio of the dominant system pole can be used as a monitoring parameter to prevent the occurrence of chatter before the system becomes unstable. The performance of the presented method was studied using numerical simulations and an experimental case study. The method was shown to successfully identify the structural poles of the system when the cut is close to the border of stability. When the cut is highly stable or when the harmonics of spindle rotation frequency coincides with one of the modal frequencies of the system, the presented method cannot identify the structural poles. However, monitoring the process for chatter occurrence is not critical in those highly stable points.

5.1 Future work

In order to use the presented approach as online chatter monitoring system, the OMA algorithm needs to be automated and its computational time needs to be reduced. Automated OMA is an active research and substantial progress have been made in the application of automated OMA for structural health monitoring [41]. While modification of the presented approach for online monitoring of chatter remains a subject for future studies, the presented approach can be used in its current offline form to quantify the stability of machining processes. This capability is particularly useful in machining chatter research where the accuracy of the developed stability lobe diagrams is verified according to the stable and unstable cutting conditions that are identified through machining experiments. In those machining experiments, usually, sound, vibration, and force signals or surface roughness analysis are used to determine if the cut is stable or unstable. The border between stable and unstable cutting parameters determined from the machining experiments are then compared against the stability lobe diagrams. Although such tests provide an approximation of the border between stable and unstable machining parameters, they don't provide any information about the dynamics of the system when it is stable, nor do they provide any numerical metric of the level of stability of the system. The dominant closed-loop system poles that are identified using the presented approach can be used not only to determine the border between stable and unstable machining parameters but also to determine the damping and frequency of the dominant poles that governs the dynamics of the system when it is stable. Also, the damping of the dominant pole can be used as a numerical metric to evaluate the stability of the system.

Bibliography

[1] Randall J Allemang and David L Brown. Experimental modal analysis and dynamic component synthesis. volume 3. modal parameter estimation. Technical report, CINCINNATI UNIV OH DEPT OF MECHANICAL AND INDUSTRIAL ENGINEERING, 1987.

[2] Matthew S. Allen, Michael W. Sracic, Shashank Chauhan, and Morten Hartvig Hansen. Output-only modal analysis of linear time-periodic systems with application to wind turbine simulation data. *Mechanical Systems and Signal Processing*, 25(4):1174–1191, 2011.

[3] Y Altintas. *Manufacturing automation*. Cambridge university press, 2012.

[4] Y. Altintas, M. Eynian, and H. Onozuka. Identification of dynamic cutting force coefficients and chatter stability with process damping. *CIRP Annals - Manufacturing Technology*, 57(1):371–374, 2008.

[5] Y. Altintaş and E. Budak. Analytical Prediction of Stability Lobes in Milling. *CIRP Annals - Manufacturing Technology*, 44(1):357–362, 1995.

[6] J. S. Bendat and A. G. Piersol. *Engineering applications of correlation and spectral analysis*. 1980.

[7] A. Brandt. A signal processing framework for operational modal analysis in time and frequency domain. *Mechanical Systems and Signal Processing*, 115:380–393, 2019.

[8] A. Brandt, M. Berardengo, S. Manzoni, and A. Cigada. Scaling of mode shapes from operational modal analysis using harmonic forces. *Journal of Sound and Vibration*, 407:128–143, 2017.

[9] A. Brandt, M. Berardengo, S. Manzoni, M. Vanali, and A. Cigada. Global scaling of operational modal analysis modes with the OMAH method. *Mechanical Systems and Signal Processing*, 117:52–64, 2019.

[10] Anders Brandt. A signal processing framework for operational modal analysis in time and frequency domain. *Mechanical Systems and Signal Processing*, 115:380–393, 2019.

[11] Ventura C Brincker, R. *Introduction to Operational Modal Analysis*. John Wiley & Sons, 2015.

[12] David L Brown, Randall J Allemang, Ray Zimmerman, and Mq Mergeay. Parameter estimation techniques for modal analysis. *SAE transactions*, pages 828–846, 1979.

[13] J Busturia and J Gimenez. Multiexcitation multiresponse non-linear least squares algorithm. *Proc. 10-th ISMA*, 1985.

[14] Hongrui Cao, Kai Zhou, and Xuefeng Chen. Chatter identification in end milling process based on eemd and nonlinear dimensionless indicators. *International Journal of Machine Tools and Manufacture*, 92:52 – 59, 2015.

[15] Roy R Craig Jr, Andrew J Kurdila, and Hyoung M Kim. State-space formulation of multi-shaker modal analysis. 1987.

[16] Congying Deng, Jianguo Miao, Yi Feng, and Bo Wei. Robust evaluation of chatter stability for milling process with uncertainties based on optimal configuration of machining position and spindle speed. *The International Journal of Advanced Manufacturing Technology*, pages 1–15, 2018.

[17] Ye Ding, LiMin Zhu, XiaoJian Zhang, and Han Ding. A full-discretization method for prediction of milling stability. *International Journal of Machine Tools and Manufacture*, 50(5):502–509, 2010.

[18] Zoltan Dombovari. Dominant modal decomposition method. *Journal of Sound and Vibration*, 392:56–69, 2017.

[19] D. J. Ewins. *Modal Testing*. Research studies press Letchworth, 1984.

[20] Svend Gade, Nis B Møller, Henrik Herlufsen, and Hans Konstantin-Hansen. Frequency Domain Techniques for Operational Modal Analysis. *First International Operational Modal Analysis Conference*, (Type 7760):261–271, 2005.

[21] Vincent Gagnol, Thien Phu Le, and Pascal Ray. Modal identification of spindle-tool unit in high-speed machining. *Mechanical Systems and Signal Processing*, 25(7):2388–2398, 2011.

[22] Tamás Insperger and Gábor Stépán. *Semi-discretization for time-delay systems: stability and engineering applications*, volume 178. Springer Science & Business Media, 2011.

[23] Niels-Jørgen Jacobsen. Separating Structural Modes and Harmonic Components in Operational Modal Analysis. *Proceedings IMAC XXIV Conference*, 2006.

[24] S.A. Jensen and Y.C. Shin. Stability analysis in face milling operations, Part 1: Theory of stability lobe prediction. *Journal of Manufacturing Science and Engineering, Transactions of the ASME*, 121(4):600–605, 1999.

[25] RS Pappa JN Juang. An eigensystem realization algorithm for modal parameter identification and model reduction. *Journal of guidance, control, and dynamics*, 1985.

[26] Adam K. Kiss, David Hajdu, Daniel Bachrathy, and Gabor Stepan. Operational stability prediction in milling based on impact tests. *Mechanical Systems and Signal Processing*, 103:327 – 339, 2018.

[27] M. Lamraoui, M. Thomas, M. El Badaoui, and F. Girardin. Indicators for monitoring chatter in milling based on instantaneous angular speeds. *Mechanical Systems and Signal Processing*, 44(1):72 – 85, 2014. Special Issue on Instantaneous Angular Speed (IAS) Processing and Angular Applications.

[28] F Lembregts, J Leuridan, and Hendrik Van Brussel. Frequency domain direct parameter identification for modal analysis: state space formulation. *Mechanical Systems and Signal Processing*, 4(1):65–75, 1990.

[29] Bin Li, Bo Luo, Xinyong Mao, Hui Cai, Fangyu Peng, and Hongqi Liu. A new approach to identifying the dynamic behavior of CNC machine tools with respect to different worktable feed speeds. *International Journal of Machine Tools and Manufacture*, 72:73–84, 2013.

[30] Zhongqun Li, Zhikang Yang, Yuerong Peng, Fan Zhu, and Xingzu Ming. Prediction of chatter stability for milling process using Runge-Kutta-based complete discretization method. *International Journal of Advanced Manufacturing Technology*, 86(1-4):943–952, 2016.

[31] Lei Ma, Shreyes N Melkote, and James B Castle. A Model-Based Computationally Efficient Method for On-Line Detection of Chatter in Milling. *Journal of Manufacturing Science and Engineering*, 135(3):31007–31011, 2013.

[32] Asia Maamar, Maher Abdelghani, Thien-Phu Le, Vincent Gagnol, and Laurent Sabourin. Operational modal identification in the presence of harmonic excitation. *Applied Acoustics*, 147:64 – 71, 2019. Special Issue on Design and Modelling of Mechanical Systems conference CMSM'2017.

[33] N.M.M. Maia and J.M.M. Silva. *Theoretical and Experimental Modal Analysis*. Engineering dynamics series. Research Studies Press, 1997.

[34] S. D. Merdol and Y. Altintas. Multi Frequency Solution of Chatter Stability for Low Immersion Milling. *Journal of Manufacturing Science and Engineering*, 126(3):459, 2004.

[35] P. Mohanty and D. J. Rixen. Operational modal analysis in the presence of harmonic excitation. *Journal of Sound and Vibration*, 270(1-2):93–109, 2004.

[36] Hamed Moradi, Gholamreza Vossoughi, Mohammad R. Movahhedy, and Hassan Salarieh. Suppression of nonlinear regenerative chatter in milling process via robust optimal control. *Journal of Process Control*, 23(5):631 – 648, 2013.

[37] Jinbo Niu, Ye Ding, Limin Zhu, and Han Ding. Runge-Kutta methods for a semi-analytical prediction of milling stability. *Nonlinear Dynamics*, 76(1):289–304, 2014.

[38] C. G. Ozoegwu. Least squares approximated stability boundaries of milling process. *International Journal of Machine Tools and Manufacture*, 79:24–30, 2014.

[39] C. G. Ozoegwu, S. N. Omenyi, and S. M. Ofochebe. Hyper-third order full-discretization methods in milling stability prediction. *International Journal of Machine Tools and Manufacture*, 92:1–9, 2015.

[40] Bart Peeters and Guido De Roeck. Reference-based stochastic subspace identification for output-only modal analysis. *Mechanical Systems and Signal Processing*, 13(6):855–878, 1999.

[41] Edwin Reynders, Jeroen Houbrechts, and Guido De Roeck. Fully automated (operational) modal analysis. *Mechanical Systems and Signal Processing*, 29:228–250, 2012.

[42] G. Stépán P. V. Bayly T. Insperger, B. P. Mann. Stability of up-milling and down-milling, part 1: alternative analytical methods. *International Journal of Machine Tools and Manufacture*, 43(1):25–34, 2003.

[43] Aijun Tang and Zhanqiang Liu. Three-dimensional stability lobe and maximum material removal rate in end milling of thin-walled plate. *International Journal of Advanced Manufacturing Technology*, 43(1-2):33–39, 2009.

[44] J. Tlusty and M. Polacek. The Stability of Machine Tools Against Self Excited Vibrations in Machining. *International Research in Production Engineering*, pages 465–474, 1963.

[45] J. Tlusty, W. Zaton, and F. Ismail. Stability Lobes in Milling. *CIRP Annals - Manufacturing Technology*, 32(1):309–313, 1983.

[46] S A Tobias. Machine tool vibration research. *International Journal of Machine Tool Design and Research*, 1(1–2):1–14, 1961.

[47] S.A. Tobias and W. Fishwick. The chatter of lathe tools under orthogonal cutting conditions. *Transaction of ASME*, 80:1079–1088, 1958.

[48] Niels Troldborg and Jn Sørensen. A simple atmospheric boundary layer model applied to large eddy simulations of wind turbine wakes. *Wind Energy*, 17(April 2013):657–669, 2014.

[49] Herman Van der Auweraer, Raymond Snoeys, and J Leuridan. A global frequency domain modal parameter estimation technique for mini-computers. *Journal of Vibration and Acoustics-Transactions of the ASME*, 1986.

[50] Peter Van Overschee and Bart De Moor. Choice of state-space basis in combined deterministic-stochastic subspace identification. *Automatica*, 31(12):1877–1883, 1995.

[51] P Verboven, P Guillaume, B Cauberghe, E Parloo, and S Vanlanduit. Frequency-domain generalized total least-squares identification for modal analysis. *Journal of Sound and Vibration*, 278(1-2):21–38, 2004.

[52] Harvard Vold, John Kundrat, G Thomas Rocklin, and Richard Russell. A multi-input modal estimation algorithm for mini-computers. *SAE Transactions*, pages 815–821, 1982.

[53] Z. Yan, X. Wang, Z. Liu, D. Wang, Y. Ji, and L. Jiao. Orthogonal polynomial approximation method for stability prediction in milling. *International Journal of Advanced Manufacturing Technology*, 91(9-12):4313–4330, 2017.

[54] I. Zaghbani and V. Songmene. Estimation of machine-tool dynamic parameters during machining operation through operational modal analysis. *International Journal of Machine Tools and Manufacture*, 49(12-13):947–957, 2009.

[55] Zhao Zhang, Hongguang Li, Guang Meng, and Chong Liu. A novel approach for the prediction of the milling stability based on the Simpson method. *International Journal of Machine Tools and Manufacture*, 99:43–47, 2015.